PHYSICAL REVIEW D **88,** 064051 (2013)

Eccentric black hole mergers and zoom-whirl behavior from elliptic inspirals to hyperbolic encounters

Roman Gold[1,2] and Bernd Brügmann[1]

[1]*Theoretical Physics Institute, University of Jena, 07743 Jena, Germany*
[2]*Department of Physics, University of Illinois at Urbana-Champaign, Urbana, Illinois 61801, USA*
(Received 20 September 2012; published 25 September 2013)

We perform a parameter study of nonspinning, equal- and unequal-mass black hole binaries on generic, eccentric orbits in numerical relativity. The linear momentum considered ranges from that of a circular orbit to ten times that value. We discuss the different manifestations of zoom-whirl behavior in the hyperbolic and the elliptic regime. The hyperbolic data set applies to dynamical capture scenarios (e.g., in globular clusters). Evolutions in the elliptic regime correspond to possible end states of supermassive black hole binaries. We spot zoom-whirl behavior for eccentricities as low as $e \sim 0.5$, i.e., within the expected range of eccentricities in massive black hole binaries from galaxy mergers and binaries near galactic centers. The resulting gravitational waveforms reveal a rich structure, which will effectively break degeneracies in parameter space, improving parameter estimation.

DOI: 10.1103/PhysRevD.88.064051 PACS numbers: 04.25.D−, 04.25.dg, 04.70.Bw, 95.30.Sf

I. INTRODUCTION

Zoom-whirl orbits arise as a general-relativistic phenomenon of the two-body problem. Such orbits do not exist in Newtonian gravity, where the orbits are Kepler's conic sections. Hence, they represent an important facet of one of the fundamental problems in general relativity (GR). The term zoom-whirl was first used in Refs. [1,2]. It refers to the orbits of eccentric binaries where tight and fast revolutions (the whirls) are separated by phases in which the two objects move out to larger distances and back in (the zooms).

The physics behind this effect is precession. For bound orbits, one can define the rate of precession as precession per orbit by measuring the angle between two consecutive apocenters. In general, precession accumulates continuously (with respect to some external reference frame) and amounts to an excess angle beyond the Newtonian motion. Precession is strongest for small separations and is therefore significant especially for eccentric orbits. In the Solar System, the precession of the orbit of Mercury due to general relativity is 43 arcseconds per century, or $(2.9 \times 10^{-5})°$ per orbit. For binary pulsars, precession is not necessarily much larger. For the Hulse-Taylor pulsar the precession is 4.2° per year, but due to its short orbital period this amounts to $(3.7 \times 10^{-3})°$ per orbit. Observed precessions are on the order of $(2 \times 10^{-2})°$ per orbit in some cases [3–5]. A supermassive black hole binary model [6,7] fitted to the optical light curve of the quasar OJ-287 predicts (model-dependent) orbital parameters with a precession as large as ∼40° per orbit.

In theory, general-relativistic orbits with even larger precessions can be easily constructed by choosing appropriate orbital parameters. This is possible for test particles following geodesics around a black hole (BH), but also for comparable-mass compact objects in the post-Newtonian (PN) approximation [8]. As long as the particle or compact object orbits well outside the innermost stable circular orbit (ISCO), the classical picture of a slowly precessing ellipse or hyperbola applies. If the orbital parameters are chosen such that the object approaches distances close to or even inside the ISCO, it may follow an unstable circular orbit for some time. After this it either plunges or escapes to larger distances (infinity if the motion is unbound), which is the zoom-whirl behavior we are interested in. In the whirl regime orbits exhibit extreme precession with precession angles comparable to or larger than 2π, wrapping the inner part of the orbit once or even several times around its center.

The basic features of zoom-whirl orbits were first discussed in the context of geodesics in a stationary black hole spacetime (e.g., Refs. [9–12]), in extreme mass-ratio inspirals (e.g., Refs. [1,13–15]), and PN evolutions [16,17]. In these contexts zoom-whirl orbits arise when the test particles move near or at the maximum of the effective potential associated with its radial motion; see, e.g., Ref. [10]. For geodesics, it is a matter of fine-tuning the initial parameters of the orbit to obtain a certain number of whirls. In fact, for geodesics the number of whirls can be made arbitrarily large since there is no gravitational radiation; see Ref. [11] for an example with six orbits during a whirl. Going beyond the test-mass limit, including radiation loss is a key task (e.g., Refs. [1,18,19]).

The main question about zoom-whirl orbits in full GR is how the classic, well-known picture of zoom-whirl geodesics changes for binaries with comparable masses in configurations where radiation damping becomes significant. Naively, we do not expect the binary to radiate away more than its total mass, i.e., the number of orbits is finite since it is limited by the energy and angular momentum radiated away during each whirl. In fact, for comparable masses one might have questioned whether it is possible to obtain even a single (full) whirl. Since the whirls happen at high velocity and small separation (even inside the

innermost stable circular orbit), the PN approximation is not directly applicable; see, e.g., Ref. [8]. However, recently some groups have performed numerical evolutions in full general relativity of eccentric black hole binaries (BHBs). Zoom-whirl orbits have indeed been found, although the number of whirls in these experiments is less than three.

In Ref. [20], Pretorius and Khurana presented the first example of a whirl orbit for an equal-mass binary. In Refs. [21–25], several examples for the transition from inspiral to plunge, radiated energy, angular momentum, and the resulting final spin were investigated. In Ref. [26] longer evolutions of unequal masses and nonvanishing spin with up to three elliptic orbits which transition through the zoom-whirl regime prior to merger were studied. The notion of marginally stable circular orbits in background spacetimes was shown to be in close resemblance to whirl orbits in numerical evolutions of finite mass ratio [10,20]. The consequences for kicks were addressed in Ref. [27]. Implications for data analysis were studied in, e.g., Refs. [28–33]. In particular, Refs. [30,31] pointed out the potentially deteriorating effects in signal processing when eccentricity is ignored in the waveform models.

Eccentric neutron-star and mixed binaries in dynamical spacetime have been studied in Refs. [34–37], and in all cases zoom-whirl behavior has been identified. The focus in Refs. [38–42] was on high-energy collisions. Among the key results so far is that the total energy radiated can easily exceed the 4% of the total mass radiated during the last stage of a quasicircular inspiral. For high-energy collisions, total radiated energies up to $35 \pm 5\%$ have been found [40]. In Ref. [24], we found at low momentum multiple extrema in the radiated energy as a function of the initial data, and that only a modest amount of fine-tuning is required to spot these extrema. These extrema should be compared to the variations in the mass and spin of the merger remnant noted in Ref. [25].

Choosing different initial data and also different tuning strategies, these investigations have been performed in different regions in parameter space. In the present work we focus on an area that has received relatively little attention so far, namely intermediate momenta and comparable but not necessarily equal masses. We extend the discussion of Ref. [24]; specifically, we consider mass ratios of 1:1, 1:2, and 1:3, and linear momenta that are 1 to 6, and in one case 10 times the value of a circular orbit, although not in all possible combinations.

Zoom-whirl is sometimes thought to occur beyond a certain, rather large eccentricity. Our results instead show that whirls can also be found for modest eccentricities. We give an analysis of the gravitational waves (GWs) and how specific features in the radiated energy are related to orbital characteristics.

A prerequisite for zoom-whirl orbits is eccentricity. *Isolated* black hole binaries formed at typical separations perform a sufficiently large number of orbits such that the orbits become circularized long before entering the strong-field regime [43]. However, it cannot be expected that all binary GW sources are sufficiently isolated and hence other effects have to be taken into account. In fact, supermassive black hole binaries are expected to be formed in gas-/star-rich environments [44] with potentially large eccentricities [45,46]. It is well understood that such binaries can gain eccentricity as a consequence of gravitational torques exchanged with the circumbinary disk [44,47–50]. Likewise, gravitational interactions with additional bodies (Kozai-oscillations, Hill-mechanism, mass segregation, gravitational focusing, etc.) generically induce eccentricity growth on a binary system. Numerous studies of such effects [28–30,51–65] suggest that the eccentricity of binaries, which emit significant gravitational radiation, cannot in general be ignored. Event-rate estimates for eccentric compact-object binaries [56,57,66] suffer from large uncertainties and vary considerably. Some studies predict that advanced LIGO should detect such sources, but given the large uncertainties this should be taken with care. For third generation detectors the detection range will be larger. Eccentric binary mergers will therefore become more interesting sources in the future. For supermassive BHBs, pulsar timing arrays will soon be able to resolve individual sources in a regime where many binaries are still expected to be eccentric [67].

Given a population of eccentric binaries, whether zoom-whirl orbits are of relevance to gravitational-wave astronomy depends on several factors. Even if the signals are stronger, if excessive fine-tuning is required, then the population of strong sources might amount to a very small corner of parameter space. Conversely, if little tuning is involved, then zoom-whirl orbits can be potential GW sources even for ground-based detectors [28–30,53]. With regard to GWs, for comparable-mass binaries with astrophysical momenta we loose the unlimited number of whirl orbits due to gravitational radiation, but what is lost corresponds to a very small part of parameter space anyway. In any case, as a matter of principle we should be prepared to detect and recognize GWs from all corners of parameter space including zoom-whirl orbits.

The paper is organized as follows. In Sec. II we describe the basics of our numerical methods, our choice of initial configurations, and give error estimates for typical runs. We discuss orbital properties in Sec. III A, resulting waveforms and radiated energy in III B, and phase-space trajectories in III C. We conclude with Sec. IV.

II. NUMERICAL METHODS AND SUMMARY OF SIMULATIONS

A. Method

We perform a parameter study of the black-hole-binary problem using three-dimensional numerical simulations obtained with the BAM code [68–70]. Initial data for black holes is computed by the puncture method [71] using a

pseudospectral code [72], and evolved with the χ variant of the moving-puncture [73,74] version of the Baumgarte-Shapiro-Shibata-Nakamura [75,76] formulation of the 3 + 1 Einstein evolution equations. We use a fourth-order Runge-Kutta method for the time integration and sixth-order finite differencing in space. The wave extraction and the calculation of the radiated energy is done using a fourth-order accurate implementation of the Newman-Penrose formalism. We extract Ψ_4 (for details see Ref. [68]) and thus also $E_{\rm rad}$ at extraction radii of $r_{\rm GW} = 60M, 80M, 100M$, where M is the total puncture mass (see below). Our grid is a box of typically $\gtrsim (640M)^3$ in size, which is sufficient to keep the boundaries causally disconnected from the GWs for most of our runs. We employ bitant or quadrant symmetry when possible. Usually, the grid consists of nine levels of mesh refinement, starting at the coarsest level with a resolution of $h = 5M$ and increasing by factors of two, resulting in a resolution of $h \approx M/50$ at the finest level. The inner, finer levels are evolved according to Berger-Oliger timestepping, while the outer levels do not follow the motion of the punctures and are evolved at the fixed time step given by the innermost fixed level [69,77]. The fixed boxes have twice as many grid points (for a more accurate wave propagation). Since some runs have exceptional settings the parameters of our simulations are summarized in Table I. For our analysis we measure the GW emission and radiated energy [normalized to the initial Arnowitt-Deser-Misner (ADM) mass], study the shape of the event horizons, the coordinate distance over time, and how much time the binary spends at a separation D. Moreover we investigate a new way of analyzing binary evolutions, namely to look at the phase

TABLE I. List of selected runs with corresponding initial data, errors $\Delta E_{\rm rad}/E_{\rm rad}$, amplitude A [and its error (ΔA)] of $r_{\rm GW}\Psi_4$ (wherein $r_{\rm GW}$ is the extraction radius), order of convergence, and merger times t_m^α. The errors ΔA and $\Delta E_{\rm rad}$ are the differences between low- and medium-resolution models. The order of convergence is obtained from convergence tests of Ψ_4 and $E_{\rm rad}$. We note that the formal order of convergence deviates from the quoted integer values by <10%. The $3P_{\rm qc}$, $\Theta = 18°$ case reveals a convergence order >4 indicating that for this case the resolutions used are not entirely in the convergent regime. A third PN estimate [21,78] of our lowest eccentric run $1P_{\rm qc}$, $\Theta = 60°$ gives $e \approx 0.5$–0.6 (depending on which definition of e is used).

Model	$\frac{\Delta E_{\rm rad}}{E_{\rm rad}}$	$\Delta A/A$	Ord.	$t_m^\alpha[M]$
$1P_{\rm qc}$, $\Theta = 10°$	0.01	0.008	4	40.5
$1P_{\rm qc}$, $\Theta = 40°$	0.013	0.010	4	92.7
$1P_{\rm qc}$, $\Theta = 52°$	0.015	0.012	4	766
$2P_{\rm qc}$, $\Theta = 23.9°$	0.017	0.016	4	79.9
$2P_{\rm qc}$, $\Theta = 26°$	0.0013	0.002	4	∞
$3P_{\rm qc}$, $\Theta = 18°$	0.0095	0.003	5	69.4
$4P_{\rm qc}$, $\Theta = 15.6°$	0.0095	0.012	4	39.0
$10P_{\rm qc}$, $\Theta^D_{50} = 5.4°$	0.03	0.012	4	40.5

space with the coordinate velocity and the separation of the punctures (v, D) serving as generalized coordinates. The velocity of the puncture is computed from the shift as $v = \sqrt{\beta_i(x_p)\beta^i(x_p)}$, where x_p is the coordinate location of the puncture. x_p is—as a diagnostic—tracked by integrating $\partial_t x^i_p = -\beta^i(x^j_p)$ using the iterated Crank-Nicolson method, as in Ref. [73].

B. Black hole parameters

The initial data for black hole binaries is characterized by a choice of the following parameters. In this work we set the spins to zero. Input for the computation of the initial data are the parameters m_i for the (bare) puncture masses, $\vec{P}_i$ for the momenta, and $\vec{x}_i$ for the positions. The total puncture mass M is defined as $M = \sum_i m_i$. Since the global mass scale in vacuum is arbitrary, the masses can be characterized by one number, say the symmetric mass ratio denoted by $\nu = m_1 m_2/(m_1 + m_2)^2$.

We choose coordinates in which the punctures are initially located on the x axis; see Fig. 1. For equal masses we set $x_{1,2} = \pm D/2$ for a coordinate separation D. For unequal masses we leave x_1 unchanged but set $x_2 = x_1 m_1/m_2$. For the momenta we choose $\vec{P}_{1,2} = \pm\vec{P}$. This—together with the choice of $x_{1,2}$—implies that initially the center of mass is at rest and that mergers happen at the origin (except for a small merger kick due to unequal masses). Concretely, we consider momenta in the x-y plane given by their magnitude P and an angle Θ such that $\vec{P} = (-P\cos\Theta, P\sin\Theta, 0)$. Specifying the "shooting angle" Θ is equivalent to the choice of an impact parameter. The magnitude P of the momenta is chosen as a multiple of $P_{\rm qc}$, which denotes the magnitude of the momentum for a quasicircular inspiral at separation D.

Given the configuration in Fig. 1, numerical simulations are parametrized by specific choices for x_1, ν, P, and Θ. We set $x_1 = 10M$ for all runs, which implies $D = 20M$ for equal masses. For unequal masses, we position the larger mass at x_2, i.e., $m_2 > m_1$ and $|x_2| < x_1$. Most of the simulations we discuss are for equal masses ($\nu = 1/4$), but we also consider a few examples for mass ratios of 1:2 ($\nu = 2/9$) and 1:3 ($\nu = 3/16$). Following Ref. [79], for equal masses at $D = 20M$ the magnitude of the momentum for quasicircular inspiral is $P_{\rm qc} = 0.061747M$. We consider $P/P_{\rm qc} = 1, 2, \ldots, 6$, and in one example as the

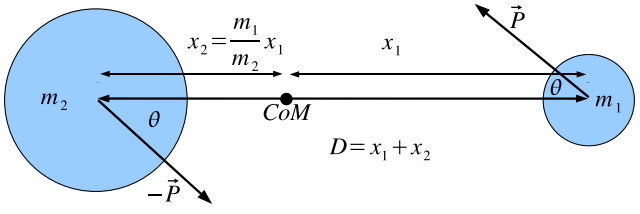

FIG. 1 (color online). Configuration of initial data.

most extreme case $P/P_{\rm qc} = 10$. The direction of the momenta is given by $\Theta \in [0, 90°]$. Here $\Theta = 0$ corresponds to a head-on collision, while for quasicircular inspiraling orbits Θ is slightly smaller than 90° because the momentum has a small radial component. The case $\Theta > 90°$ with initially radially outgoing motion can be ignored [80].

The ADM mass at the ith puncture and at infinity is

$$M^i_{\rm ADM} = (1 + u(\vec{x}_i))m_i + \frac{m_1 m_2}{2D}, \tag{1}$$

$$M^{\infty}_{\rm ADM} = M^1_{\rm ADM} + M^2_{\rm ADM} + E_{\rm bind} = m_1 + m_2 + \lim_{r\to\infty}(2ru), \tag{2}$$

respectively, where u is the correction to the conformal factor in the puncture framework and $E_{\rm bind}$ is the net binding energy. Values for $M^{\infty}_{\rm ADM}$ range from 0.994 for $1P_{\rm qc}$ to 1.2 for $6P_{\rm qc}$. Since the momenta are nonzero, we obtain larger physical masses $M^i_{\rm ADM}$ at the inner asymptotically flat ends of the punctures. The difference between the masses m_i and $M^i_{\rm ADM}$ ranges from $7 \times 10^{-3}M$ for $1P_{\rm qc}$ to $3.5 \times 10^{-2}M$ for $6P_{\rm qc}$, and is essentially independent of Θ.

For the main part of this work, we first choose a specific mass ratio; in particular, we choose between equal and unequal masses. Second, we choose one of several (low-) momentum cases. Third, we vary the shooting angle systematically, in particular searching for maxima and minima in the total radiated energy, examining the number of whirls, etc. There are some obvious alternatives to set up such parameter scans, say by fixing Θ [23], using some measure of eccentricity, the angular momentum [25], or the binding energy [21] as a parameter. Apart from having a simple interpretation as a scattering experiment with fixed momentum size, our setup also describes simulations at roughly constant total energy, if in analogy to classical point masses the total energy is defined as the sum of the kinetic and potential energy (since P and D are constant while varying Θ). Each run amounts to 500–30000 CPUh (the latter one for $1P_{\rm qc}$, $\Theta = 60°$), which is strongly dependent on how far and how many times the orbits zoom out. We implement Brent's method [81] to bracket local extrema in the efficiency of converting energy into outgoing gravitational radiation, for which a small number of runs suffices. This reduces the total number of runs to about 130 while still sampling the parameter space in an adaptive and accurate way. In retrospect, we found that a golden section search [81] is—for the finite accuracy we required—a better choice despite being only first-order convergent. The parabolic interpolation inside Brent's method chooses the new guesses systematically towards the flatter part of the asymmetric maxima.

C. Convergence and error estimates

We performed a convergence analysis for a representative subset of our runs and in general found fourth-order convergence in the 22-mode of $r\Psi_4$ and in the radiated energy $E_{\rm rad}$, demonstrating the overall consistency of the code with respect to the order of the Runge-Kutta integrator and the wave-extraction routine. The errors due to the finite radius of our wave-extraction sphere are quantified by the deviation from a $1/r$ falloff as measured from the data taken at three different extraction radii.

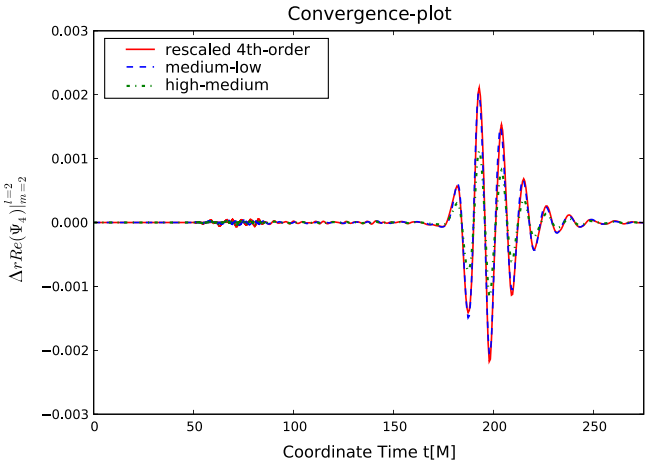

FIG. 2 (color online). Convergence plot of the 22-mode of $r\Psi_4$ for $P = 1P_{\rm qc}$, $\Theta = 40°$. The blue dashed line shows the difference of $r\mathcal{R}e(\Psi_4)|^{l=2}_{m=2}$ as computed from the medium- and low-resolution data, and the green (dashed dotted) line shows the difference from high- and medium-resolution data. The solid line rescales the latter one assuming fourth-order convergence. Both lines lie on top of each other, demonstrating the overall consistency of our results. The small noise at the beginning is due to the spurious junk radiation of conformally flat initial data.

Error estimates based on this analysis are shown in Table I, and selected convergence plots are shown in Figs. 2 and 3. In general, highly eccentric orbits are accurately treated by the BAM code, and also the presence of the rather high momenta considered here can be dealt with consistently. The relative error in the 22-mode and the radiated energy due to both the finite resolution and the extraction radius is around 1%. For larger momenta the error from a finite extraction radius becomes the dominating error ($\approx 2\%$). Increasing the initial momentum leads to higher amounts of artificial (junk) radiation, enhances the ADM mass of the initial time slice, and reduces the BH horizons. At some point these effects contaminate the solution in the sense that its physical relevance becomes questionable. However, we limited our data set to those regimes where the artificial radiation is either entirely negligible or at least small in comparison to the physical radiation. The $P = 10P_{\rm qc}$ sequence represents an exception, but we only used it in the context of the Hawking limit and as an approximate extrapolation of our data set to the ones obtained by other groups at larger momenta.

The error due to the junk radiation arising from the conformally flat initial data can be reduced to some extent by choosing a sufficiently large initial separation. In the very high-momentum case we needed both large separations and

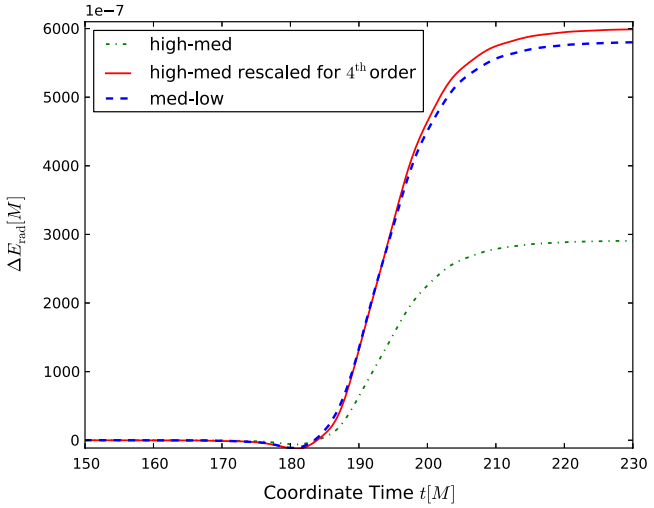

FIG. 3 (color online). Convergence plot of the radiated energy for $P = 1P_{\rm qc}$, $\Theta = 40°$. The blue dashed line shows the difference $\Delta E_{\rm rad}$ as computed from the medium- and low-resolution data, and the green (dashed dotted) line shows the difference from high- and medium-resolution data. The solid line rescales the latter one assuming fourth-order convergence. The solid red line and the dashed blue one are almost on top of each other, demonstrating a convergence order very close to four, consistent with our numerical scheme.

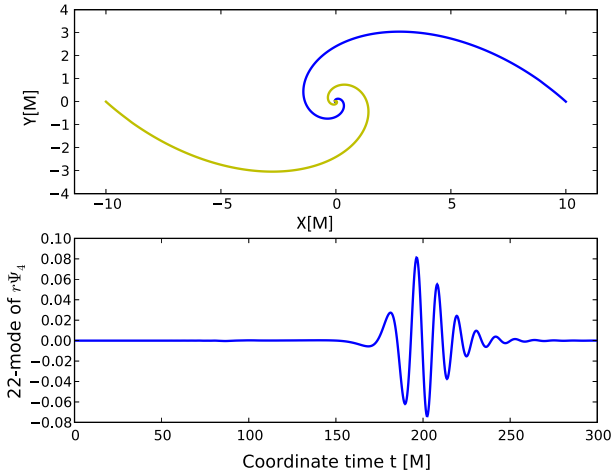

FIG. 4 (color online). $P = P_{\rm qc}$, $\Theta = 42°$: Puncture tracks (upper panel) and GW 22-mode (lower panel). From $\Theta = 0°$ to about 40°, the black holes collide within $200M$ of evolution time and perform less than one orbit before merger. The waves show a merger signal with a brief ring-up and characteristic ring-down. In the limit of the head-on collision, $\Theta \to 0°$, the 22-mode vanishes and the 20-mode becomes the dominant mode.

also much larger resolution until the radiated energy results converged, but once the appropriate resolution is used the accuracy compares favorably with the other results. For yet higher-momentum runs we refer to Refs. [38,40], who studied momenta beyond the rest-mass-dominated regime.

Convergence for unequal masses can be shown only at the higher resolutions. For the resolution we used the $l = 2$, $m = 2$ mode converges at second order—a common tendency when being at the edge of the convergent regime. The somewhat lower accuracy for larger mass ratios is a well-known effect of the gamma-driver condition we use ($\eta = $ const). In Refs. [82–84] it was shown that a generalization of this condition (with η dependent on the local mass) leads to an improvement in accuracy.

Analyzing the dependence on resolution shows that the derived errors in the energy are not behaving according to a Gaussian distribution. There is a skewness in the actual (unknown) distribution of our measurements such that higher resolutions systematically produce higher energies. Hence, our error bars should be slightly more extended towards larger values of $E_{\rm rad}$.

Summarizing, the simulations presented here do not pose new challenges to the numerical scheme, although there are specific requirements for accuracy in the presence of whirls together with long run times. In these cases there is a high sensitivity to the parameters and during the long evolutions numerical errors accumulate. Nevertheless, these evolutions have similar convergence behavior and error estimates, and only require a higher resolution to obtain convergence.

III. RESULTS

A. Orbital properties

To prime the discussion of the orbits, we first consider several examples of the coordinate tracks of the punctures for equal-mass binaries with $P = P_{\rm qc}$ and $P = 5P_{\rm qc}$; see Figs. 4–10. It is helpful to read the captions of these figures in sequence. The puncture tracks in the x-y coordinate plane are shown in the upper panels, and the 22-mode of the waveforms are shown in the lower panels. The waveforms are further discussed in Sec. III B. The figures show two sequences of runs for two momenta that explore how the orbits change when the shooting angle is varied from small to large.

1. Classification of orbits

For any choice of mass ratio ν and initial separation D, we can in principle fill in a "phase diagram," as shown in Fig. 11, which labels orbits in a P-Θ plot. The main classification is whether the initial parameters P and Θ lead to orbits that are bound (implying capture and merger) or unbound (escape to infinity). In Newtonian gravity, we only have to check whether the kinetic energy exceeds the potential energy, or equivalently whether the binding energy is positive or negative. In general relativity, this distinction is sometimes only possible *a posteriori* since the gravitational waves and the associated loss of energy and angular momentum are only known after the Einstein equations have been solved. Solutions to the evolution problem define the dividing line $P = P_{\rm bu}(\nu, D, \Theta)$ in Fig. 11. Orbits with $P > P_{\rm bu}$ are unbound, whereas orbits with $P < P_{\rm bu}$ are bound.

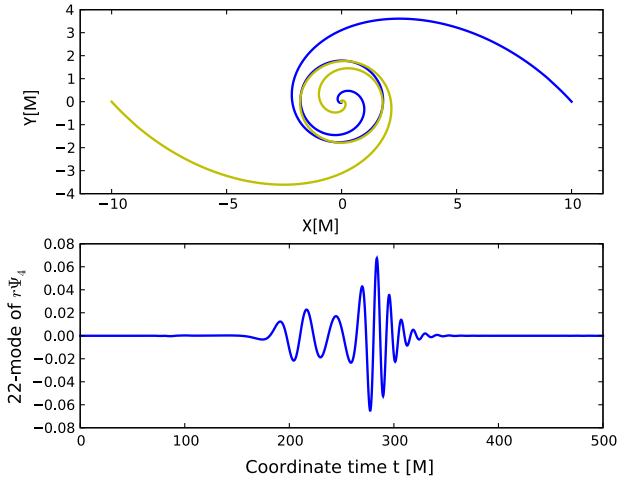

FIG. 5 (color online). $P = P_{\rm qc}$, $\Theta = 48°$: Puncture tracks (upper panel) and GW 22-mode (lower panel). There is about one full whirl in a range of $\pm 1°$ around this shooting angle followed by the merger. The waveform clearly shows a wave associated with the whirl. Its amplitude is smaller than that of the ensuing merger signal. The diameter of the whirl is smaller than the innermost stable circular orbit of a Schwarzschild BH with the same total ADM mass.

A simplified, *a priori* upper limit on the momentum P that ensures boundedness is $\tilde{P}_b := P_{\rm bu}(\nu, D, \Theta = 180°)$, which is independent of Θ, cf. Fig. 11. If the momentum P does not suffice to escape in the direction $\Theta = 180°$ (for which radiation losses are minimized), then the orbits are bound for all Θ. Here we use the assumption that the black holes are not spinning. Approximating the minimal

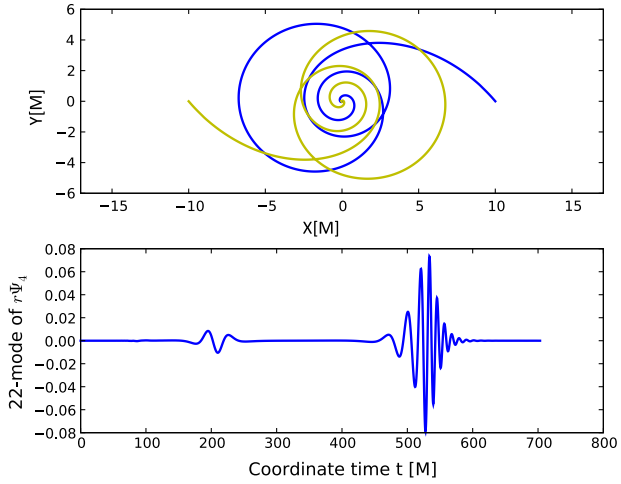

FIG. 6 (color online). $P = P_{\rm qc}$, $\Theta = 50°$: Puncture tracks (upper panel) and GW 22-mode (lower panel). For a shooting angle two degrees larger than that leading to the strong whirl, there is a close encounter with a precession of about half an orbit, followed by a zoom out to about three times the radius at pericenter, followed by a short inspiral and merger that starts with significantly reduced eccentricity. Note the comparatively small and short wave pulse associated with the close encounter, again at about $200M$ of evolution.

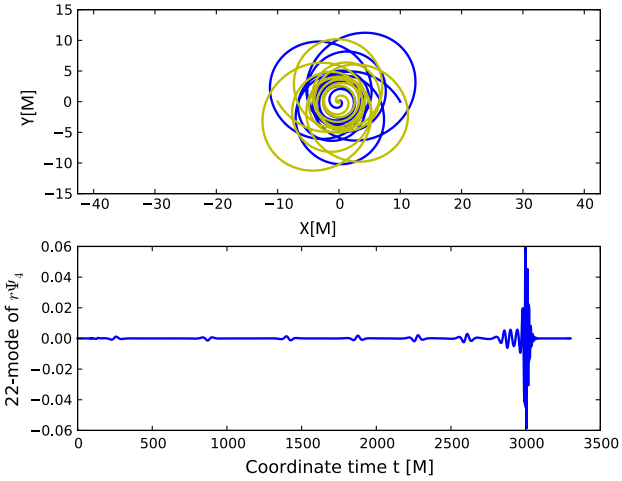

FIG. 7 (color online). $P = P_{\rm qc}$, $\Theta = 60°$: Puncture tracks (upper panel) and GW 22-mode (lower panel). Increasing the shooting angle beyond 50°, one can find an increasing number of elliptic orbits. Note that the wave pulses associated with the close encounters are smaller than, e.g., in Fig. 6 mainly because the binary separation at pericenter is larger; see Fig. 12. Early on the orbit resembles the classical picture of a (strongly) precessing ellipse. The plot shows a transition through plunge through a full whirl phase at the onset of merger with a clear corresponding wave signal.

radiation loss in the "head-off" direction as zero, we compute a simple estimate of $\tilde{P}_b$ based on the binding energy in Eq. (2). Fixing $\Theta = 180°$ and $D = 20M$ we iteratively compute initial data with varying P to obtain the binding energy $E_{\rm bind}$. $\tilde{P}$ is then defined as $\tilde{P} := P(E_{\rm bind} = 0, \Theta = 180°)$, resulting in $\tilde{P} = 0.085(4 \pm 3)M$.

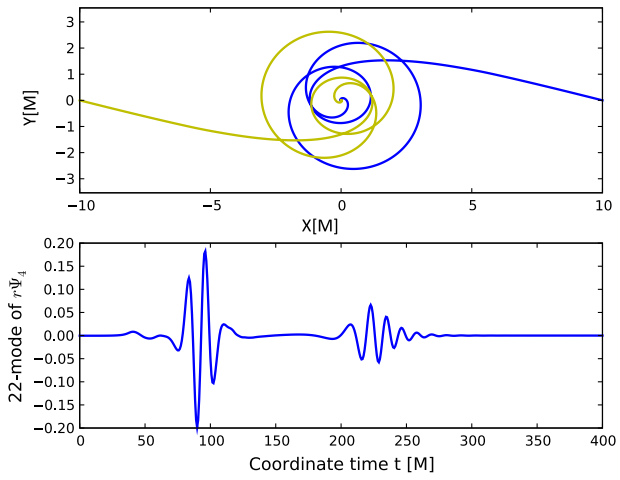

FIG. 8 (color online). $P = 5P_{\rm qc}$, $\Theta = 14.15°$: Puncture tracks (upper panel) and GW 22-mode (lower panel). This example is for an initial momentum that is significantly larger than that of quasicircular orbits, and which can easily produce unbound orbits. Zoom-whirl orbits are found for much smaller shooting angles than in Figs. 4–7. There is one whirl and a short zoom followed by a merger. Due to the additional kinetic energy, the whirl signal increases in amplitude and exceeds the merger signal.

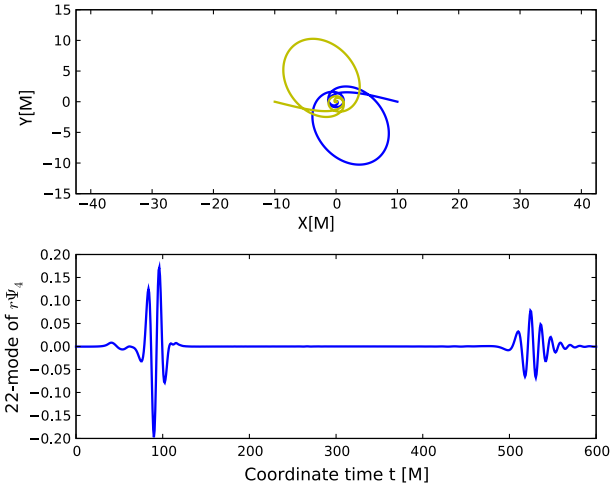

FIG. 9 (color online). $P = 5P_{\rm qc}$, $\Theta = 14.20°$: Puncture tracks (upper panel) and GW 22-mode (lower panel). The larger the momentum, the more sensitive the orbit becomes to the choice of the shooting angle. A small change in angle compared to Fig. 8 leads to a much larger zoom out to an apocenter distance of $12M$, before it merges at the next encounter. The initial whirl, however, is almost unchanged, highlighting the analogy to unstable circular orbits.

There is some error since we end the iteration at some point, since radiation effects are ignored, and due to the finite initial separation. For example, the momentum of the quasicircular orbit leads to bound orbits for all angles since $P_{\rm qc} < \tilde{P} \approx 1.377 P_{\rm qc}$.

For brevity, we will refer to the set of configurations satisfying $P < \tilde{P}$ as the *elliptic* regime. On the other hand, orbits with $P > \tilde{P}$ form the *hyperbolic* class. Note that this terminology skips over the fact that orbits in the hyperbolic regime may still lead to a merger provided Θ is small enough.

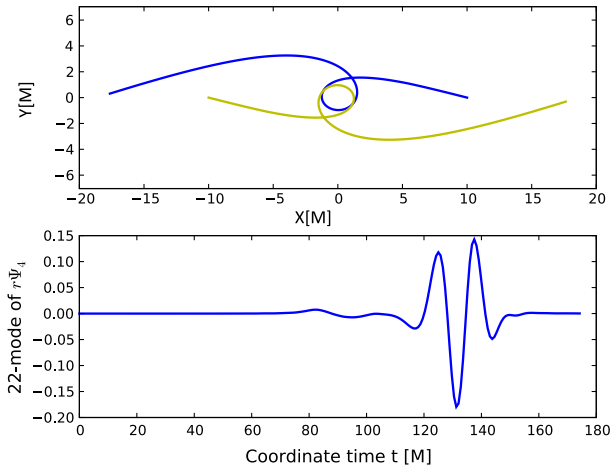

FIG. 10 (color online). $P = 5P_{\rm qc}$, $\Theta = 14.30°$: Puncture tracks (upper panel) and GW 22-mode (lower panel). Enlarging the shooting angle further compared to Fig. 9 results in a full whirl followed by a zoom to infinity (unbound orbit, no merger).

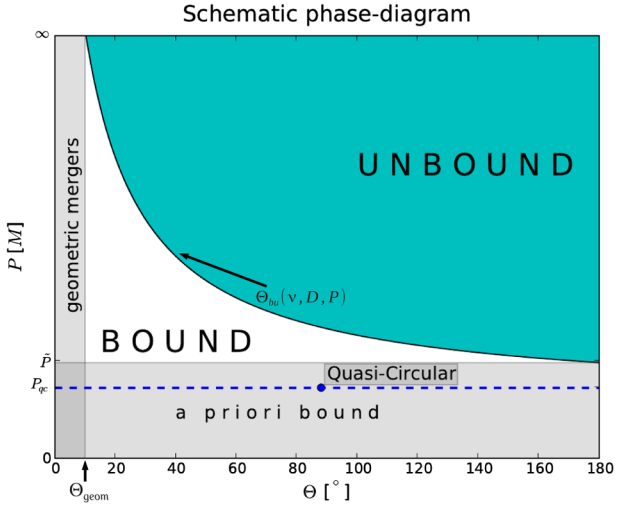

FIG. 11 (color online). This plot sketches the end state of eccentric black hole binaries in the plane spanned by our parameter choice for the initial data. The evolutions located in the gray shaded regions can be judged to be bound solely based on the initial data.

Inverting $P_{\rm bu}(\nu, D, \Theta)$, we define $\Theta_{\rm bu}(\nu, D, P)$, the shooting angle between bound and unbound orbits, as a function of P. An *a priori* lower limit for bound orbits is given by $\Theta_{\rm geom} = \Theta_{\rm bu}(\nu, D, P = \infty)$; see Fig. 11. In practice it is tricky to study large P due to limitations in the construction of initial data. Conceptually, however, we can think of this limit as a geometric constraint based on the finite size of the black holes, i.e., the idea is that the two black holes must merge when their event horizons touch. Using Euclidean geometry, i.e., assuming the BHs move on a straight line, a lower bound for $\Theta_{\rm geom}$ at any given ν, D, and P is given by $\sin(\Theta_{\rm geom}) = d_{\rm merger}/D$, where $d_{\rm merger}$ is the separation of the punctures at the time of the merger. However, the size of the black holes depends on the gauge. The Schwarzschild radius for a mass m is $2m$ in Schwarzschild coordinates, $m/2$ for isotropic coordinates, and depending on the moving puncture gauge somewhere in between for the numerical evolutions. We therefore use the numerical result for $d_{\rm merger}$. For equal masses we find that a common event horizon appears at a coordinate distance of about $d_{\rm merger} \approx 1.76$ to $1.95M$ (with a slight drift towards smaller values with increasing momentum). For an initial separation of $D = 20M$ This estimate leads to a geometric limit of $\Theta_{\rm geom} = 10.5°$ using the Euclidean formula. This limit does not appear to be very restrictive for low momenta, but it is not in contradiction to the runs of this study, either. All our simulations with $\Theta < \Theta_{\rm geom}$ end in a merger.

Another possible estimate to derive lower limits on $\Theta_{\rm bu}$ uses geodesics. (The corresponding values from our evolutions can be seen as a vertical dividing line in Figs. 15, 17, and 18.) Since we find that $\Theta_{\rm bu}$ decreases monotonically with increasing P, we expect this lower

limit to be most restrictive for large P. The idea is analogous to the capture/escape cavities for a photon in Schwarzschild spacetime in Ref. [85].

A null geodesic in the Schwarzschild spacetime on a circular orbit is located at a radius equal to the so-called photon orbit $r_{\rm photon} = 3m$, which leads to the limit

$$\Theta_{\rm bu}^{\rm geod} = \arctan\left(\frac{r_{\rm photon}}{2D}\right) \approx 16.7°.$$

The proper computation of a null geodesic in Schwarzschild spacetime [85] leads to

$$\Theta_{\rm bu}^{\rm geod} = 180° - \arcsin\left(\frac{3\sqrt{3}m}{D/2}\sqrt{1-\frac{2m}{D/2}}\right) = 27.7°.$$

The same calculation for marginally bound circular orbits yields 21.8°. Figure 17 indicates that neither of these limits apply to our evolutions, because there are unbound orbits with $\Theta < \Theta_{\rm bu}^{\rm geod}$. Clearly, the assumption of a Schwarzschild spacetime is not a good one.

From Refs. [23,25] we know that the merger remnant in our settings will settle down to a Kerr solution with spin parameters between $0.6 < a < 0.823$ with only a weak dependence on the initial conditions. Despite the fact that the Kerr metric does not describe the spacetime *at* merger, it may be a better approximation than Schwarzschild. The same estimate as above but assuming a Kerr spacetime yields $\Theta_{\rm bu}^{\rm geod} = 14.9°$ for $a = 0.6$, $\Theta_{\rm bu}^{\rm geod} = 11.4$ for $a = 0.823$, and $\Theta_{\rm bu}^{\rm geod} = 5.7°$ for $a = 1$. The Θ values for $0.6 \leq a \leq 0.823$ correspond rather well to the shooting angles separating bound from unbound runs in the higher-momentum cases despite the fact that the limit from null geodesics to (finite-size) equal-mass binaries is by no means straightforward. We will use this analogy in interpreting our results on the radiated energy in Sec. III B 2 based on the tightening of the whirl orbits associated with a larger spin of the merger remnant.

The determination of the ultimate fate of a system outside the above ranges requires a full numerical evolution. Here a bound system can be defined by the (future) formation of a single event horizon, which is expensive to compute numerically. In our evolutions we use a criterion on the lapse at the center of our grid to determine a merger time. We justify this approach by a direct comparison with an event-horizon finder [86,87]. The merger time t_m is approximated by t_m^α, the time by which the lapse at the center of our grid has dropped below $\alpha = 0.3$. This is near the analytical value of a single Schwarzschild black hole in the same and similar gauges [88–90]. We have chosen a moderately long evolution among the elliptic category and get $t_m = 484.175M$ and $t_m^\alpha = 485.524$. Therefore, we infer that using t_m^α as an estimate for t_m is accurate to within $\Delta t_m/t_m = 0.0028$ (for this case). We should mention, however, that the lapse criterion gives worse answers when the punctures move too fast, because the value $\alpha = 0.3$ is motivated by a Schwarzschild spacetime and hence is not well adapted to a boosted black hole. We used the lapse criterion to estimate the merger times and list them in Table I. These values are also used in Figs. 19 and 20.

Even if one performs a numerical evolution it can be difficult to determine whether an orbit is unbound. The absence of a common horizon is only a necessary but not a sufficient condition for unboundedness. If a merger does not occur after a given finite time, the question is how long the simulation must be continued in order to settle whether the binary is bound or unbound, and in principle this time can be infinite. A practical, approximate criterion can be given in terms of the initial binding energy $E_{\rm bind}$ and the energy radiated in GWs (see Sec. III B) during the first encounter. Without gravitational radiation $E_{\rm bind}$ is a constant of motion and the orbits are unbound for $E_{\rm bind} > 0$ and bound if $E_{\rm bind} < 0$. We find, unsurprisingly, that all orbits with $E_{\rm bind} < 0$ also merge in our evolutions. We judge an orbit to be dynamically captured when the energy radiated during the first encounter exceeds the initial (positive) binding energy. This shortens the run time to determine whether a run is unbound significantly because we do not have to track the black holes to larger and larger distances. Such a criterion is applicable close to the threshold between bound and unbound runs, although a few marginally bound runs may be incorrectly labeled unbound (but runs are labeled bound correctly).

We conclude with remarks on the relation to periodic orbits. Within the category of bound orbits there is a detailed classification scheme based on periodic orbits which is complete when neglecting radiation effects. In this classification [12,16] one indexes all closed orbits with a triplet of integers (z, w, υ), where z is the number of zooms within an approximate 2π period of the azimuthal angle ϕ (i.e., the number of "leaves"), υ is the stride over the leaves $(1 \leq \upsilon \leq z-1)$, and w is the number of whirls. The total precession angle is $2\pi(w + \frac{\upsilon}{z})$. The question is whether this classification still works in an approximate sense for BHBs with radiation effects. Especially near the merger of comparable mass BHBs, the orbits shrink significantly and may not be well represented by a single periodic orbit, but rather by a sequence of them. Our findings imply that the longest whirls associated with the largest precession angles (largest w) occur for momenta with P slightly larger than $\tilde{P}$ and are very close to a precession of 2π. We also find that the dependence on P is weak and beyond $P \gtrsim 2P_{\rm qc}$ it is compatible with the statement that it only depends on the mass ratio. Radiation damping seems to limit the length of the whirl phase for larger P, although there may be artifacts due to the initial data. In terms of periodic tables this means that we typically find preferred subsets of periodic orbits that best approximate our evolutions. The number of whirl orbits w is clearly limited by the efficiency of gravitational radiation. For equal masses $w = 1$ seems to be the largest w one can obtain. For larger mass ratios $w = 2$ should also become possible somewhere beyond a mass ratio of 1:3.

In the regime we are probing orbits with $z = 2$, $z = 3$, and $\upsilon = 1$ are favored. However, our data set contains too few data points on different mass ratios to make a strong statement.

2. Examples for orbital dynamics of BHBs

We describe the main aspects of the orbital dynamics that we find in our data set using the categorization introduced in the previous section. First we consider equal-mass BHBs in the elliptic regime. All equal-mass runs start at $D = 20M$ ($P = 10P_{\rm qc}$ has $D = 50M$) in such a way that D shrinks. Obviously, the ensuing evolution depends on the values of P and Θ.

We discuss the orbital dynamics from low to high Θ for $P = P_{\rm qc}$. Puncture tracks for some values of Θ are shown in Figs. 4–7, while Fig. 12 shows the coordinate distance D. The insets of Fig. 14 show puncture tracks for some additional values of Θ.

At low Θ (or equivalently for high eccentricities) D monotonically shrinks, leading to a rather prompt merger without completing a single orbit (see Fig. 4). The runs with larger Θ have correspondingly higher initial orbital angular momentum and therefore manage to resist the strong gravitational pull for longer so that the merger time steadily grows. For $\Theta \approx 46°$ the punctures complete one orbit before merger. At yet larger $\Theta \gtrsim 48°$ (see Fig. 5) the orbits begin to exhibit a circular phase (the whirl) which is maintained for longer as Θ is increased. However, at $\Theta \approx 48.5°$ the orbit leaves the circle again towards larger radii (the zoom) delaying the merger significantly. In this range of Θ there is high sensitivity to the initial data (concerning merger time as a function of Θ). A mild increase in Θ leads to a much larger t_m because the BHs slow down as they move out before falling back (see, e.g., Fig. 6). In the limit $\Theta \to 90°$ the pericenter passages become shorter while the apocenters and pericenters become increasingly degenerate. The pericenter moves out with Θ, and hence the BHs do not cross their mutual gravitational potential as deeply and consequently not as much radiation occurs, enabling more and more orbits before merger.

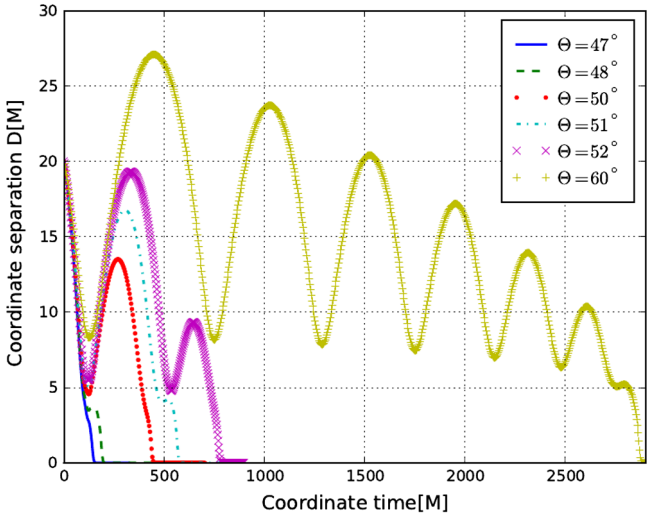

FIG. 12 (color online). Coordinate distance in the $P = 1P_{\rm qc}$ sequence as a function of time. For larger Θ more eccentric orbits in the inspiral become possible before merger. We simulated up to 6(+1) orbits for $\Theta = 60°$. Note the brief plateaus (marked by the ellipses) due to whirls before merger in the 48°, 51°, 60° cases in contrast to the short plunges in the other cases.

Concerning the amount of precession, we see that although our evolutions start somewhere after the apocenter (e.g., Fig. 14), the orbits exhibit a huge precession of roughly π and close to 2π for $\Theta = 48.5°$ (followed by a tiny zoom). Even for the smallest eccentricity we studied, $\Theta = 60°$ ($e \sim 0.5$), one can see that the ellipses still have precessions as large as $2\pi/3$, meaning that over the course of the whole evolution the accumulated precession amounts to more than two entire orbits. These values by far exceed the amounts of precession known from mildly relativistic systems, like the famous Hulse-Taylor pulsar [3] with a precession of $q = 0.0037°$ per orbit or the binary pulsar [4] with $q = 0.0044°$ per orbit.

The orbital pattern of an eccentric binary resembles a multileaf clover. However, the precession per orbit fails in general to be an exact integer fraction of 2π. This implies that the multileaf pattern will change in time. Typically the change in the rate of precession is small compared to the precession angle (per orbit). In this case the behavior of the multileaf clover can approximately be decomposed into a "stationary" component (the multileaf clover) and a rotation on top of it with a secular time scale.

This is discussed in studies of periodic orbits [12,16] (or nearby aperiodic orbits).

This effect is visible in our evolutions as well. Due to the orbital shrinkage and short evolutions this effect manifests itself not as clearly as in Refs. [12,16]. We refer to Fig. 7: a close inspection reveals that the orbital phase of the first apocenter is smaller than for the fourth one. The precession is close to $2\pi/3$ plus a small contribution leading to the orbital phase offset between leaf 1 and 4.

Switching to the hyperbolic class the additional possibility arises that the BHs just fly past each other, deflecting their trajectories and escaping to infinity. This gives rise to the merger/fly-by threshold (see insets in Fig. 15), which we will discuss later.

We again describe the orbital phenomenology from low to high values of Θ. The qualitative features of low-Θ evolutions are the same as in the elliptic category. The actual values of Θ that lead to analogous features/characteristics (one complete orbit, a whirl, maximum in $E_{\rm rad}$, etc.) decrease for increasing P. This is in agreement with the expectation that for larger P one has to shoot the BHs closer to each other compared to the corresponding

lower-P evolutions in order to obtain a qualitatively similar behavior. Again, as in the elliptic category for larger values of Θ the whirl phase is followed by a zoom. Depending on P there now is a finite range in Θ where the BHs do not escape to infinity, but reach an outer turning point (like for elliptic orbits) and fall back, ending in a delayed merger. Beyond a certain (momentum-dependent) value of $\Theta_{\rm bu}$ the BHs are simply deflected or fly by each other.

Inside the hyperbolic category, most surviving first encounters in our simulations are in the whirl regime. We only find orbits exhibiting whirls during the first encounter and never thereafter. This behavior is consistent with the interpretation that too much angular momentum is radiated during the first whirl to have another whirl episode. Another way of explaining this is to realize that the first pericenter distance during which dynamical capture occurs is already within any (quasi)stable orbit. On the next encounter the binary will have lost additional angular momentum and will have a yet smaller pericenter separation. The system therefore is likely to merge on the next encounter. It is unclear whether for high momenta there can also be cases where after a first whirl the orbital parameters fall into the narrow window for a second whirl.

In geodesic motion there exist solutions that escape to infinity after a full 2π whirl.

We also find such orbits in the comparable-mass case for sufficiently large P; see Fig. 10. For $P = 2P_{\rm qc}$ we can rule out such orbits because the deflection angles in the runs where the BHs escape to infinity are significantly smaller than 2π and are thus not in the whirl regime. This is most probably due to excessive loss of energy and angular momentum during the whirl. For larger P we find that such orbits are possible for fine-tuned initial data (as in the geodesic case).

We now give a possible explanation as to why such orbits might appear only for sufficiently large P. This behavior could be associated with the finding in Refs. [21,23,25] that the final spin first increases (and hence the innermost radius of circular orbits decreases) and then saturates for sufficiently large P. In the latter regime the whirl radius then does not decrease much further and hence the gravitational radiation during the whirl saturates as well. However, the initial kinetic energy continues to grow. Thus, for large enough P, there can be enough kinetic energy available after the whirl for the BHs to escape to infinity.

While we only find examples for $P \geq 5P_{\rm qc}$ we cannot rule out their existence for $2P_{\rm qc} < P < 5P_{\rm qc}$. It is an open question how this trend continues for yet larger momentum P.

We proceed by analyzing precession effects and discuss resemblances to periodic orbits. For a given P the precession angle shrinks with increasing Θ when approaching the threshold as expected. The maximal amount of precession we find (see Fig. 10) is slightly larger than in the elliptic category. We clearly recognize patterns known from periodic orbits. For the $P = 2P_{\rm qc}$ sequence we find $z = 2$, $z = 3$, $z = 4$ orbits. The main difference from periodic orbits is that the orbits end in a merger after the first leaf has been traversed because of the severe radiation losses. For instance the first orbits of $P = 1P_{\rm qc}$, $\Theta = 60°$ (see Fig. 7) are approximated by $z = 3$, $v = 1$, $w = 0$, while $P = 2P_{\rm qc}$, $\Theta = 25.1°$ (not shown) resembles the $z = 3$, $v = 1$, $w = 0$ orbit with $q = 2\pi/3$. When decreasing Θ by small amounts, the resulting orbits typically show the same amount of precession (only $D_{\rm per}$ shrinks with Θ). At some point there is a transition to another multileaf clover and the precession amounts to a value of $q = \pi$ and is now similar to the periodic orbit labeled $z = 2$, $w = 0$, $v = 1$.

3. Unequal-mass BHBs and the geodesic limit

Next we extend the discussion to unequal-mass BHBs. By doing so we move towards a region in parameter space which can be increasingly well described by geodesics. In fact, zoom-whirl behavior was first studied in the latter regime [1]. This raises the following question: given a binary at a finite mass ratio, how far away is it from the geodesic limit?

The fact that zoom-whirls can be found not only for geodesics but also for equal masses suggests that zoom-whirls also occur for intermediate mass ratios and adds to their expected astrophysical relevance. Indeed, we can confirm (see also Refs. [26,37]) the presence of zoom-whirl behavior for mass ratios of 1:2 ($\nu \approx 0.2222$) and 1:3 ($\nu = 0.1875$) (see Fig. 24).

As the mass ratio departs from unity, gravitational radiation decreases (see, e.g., Ref. [91]), which is consistent with the trend to the geodesic limit. In the eccentric case we find that qualitatively a similar statement still holds. We point out, though, that there is a nontrivial dependence on Θ (or inverse eccentricity). In particular, the maximum in $E_{\rm rad}/M_{\rm ADM}$ (see Sec. III B 2 and Fig. 18) is close to the equal-mass values for the mass ratios we have probed.

For lower symmetric mass ratio ν we do not find significantly longer whirl phases in our data sets. It is to be expected of course that for some mass ratio beyond 1:3 the whirl phases eventually *will* be longer and asymptote to the geodesic limit. Highly eccentric binaries with mass ratios up to 1:3 are in this sense still far away from the geodesic limit.

We find evidence for the analogy of zoom-whirl dynamics and unstable circular orbits by investigating the orbital radius during the whirl phase for various configurations. Consistently, the whirl radius decreases with increasing P, which we will refer to as the *tightening* of the whirl. This is consistent with earlier studies [21,23,25], in which it was found that the spin of the merger remnant increases with the initial angular momentum parameter until it saturates, which implies a smaller radius for the unstable circular orbits.

B. Radiation properties

1. Waveforms

The methods used to compute quantities characterizing the GW content of the spacetime are described in, e.g., Ref. [68]. Here we demonstrate how the orbital dynamics as described in Sec. III A are reflected in the GW signals.

The waveforms of quasicircular binaries are rather well understood. To a certain extent merger waveforms as they arise from evolving quasicircular binaries can be very similar to the ones seen in low-eccentricity evolutions provided the binary circularizes before merger. For large eccentricities it is, however, natural to expect deviations from a quasicircular BHB. We observe differences in the waveforms throughout the evolution, including inspiral, onset of merger, coalescence, and ring-down. Any imprints left from the eccentric inspiral have to be radiated away during this process, because the final spacetime can be described by the Kerr metric. In Ref. [24] (Fig. 2) we have compared a waveform of a quasicircular binary to the one that maximizes $E_{\rm rad}$. The largest differences occur at the onset of merger. However, the merger remnant also gives rise to a (relatively small) departure from the quasicircular case during ring-down [24]. In particular, quite generically high eccentricity is correlated with an amplified ring-down signal.

The inspiral features show some level of agreement with Ref. [92] and PN models for such waveforms are known analytically to second PN order [93] (see the first comparison between numerical waveforms and post-Newtonian ones in the eccentric regime [94]). However, features associated with zoom-whirl behavior (see Fig. 7 prior to merger) are exclusive to the strong field. Moreover, in the comparable-mass regime radiation losses and nonlinear effects become important. Thus this situation has to be dealt with using the tools of numerical relativity. These inspiral signals will be observable by future GW interferometers, such as LISA [95,96], eLISA/NGO [97], DECIGO [98], or the ET telescope [99,100].

We discuss typical waveforms of a representative subset of our evolutions. It is illustrative to go through Figs. 4–10 and 14 and their captions. Our main focus is on the richness in information stored in eccentric BHB waveforms in contrast to quasicircular ones because of the promising implications for data analysis; see Ref. [33].

Already the 22-mode shows obvious differences which become larger in other modes. For example, the $l = 2$, $m = 0$ mode of a quasicircular orbit looks just like a smaller-amplitude version of the $l = 2$ $m = 2$ mode. In the eccentric case they contain completely different features. We plot the higher-l modes summed over m in Fig. 13 for the equal-mass case, for which (without BH spin) only even-l modes contribute by symmetry. We have computed the $l \leq 8$ modes and find that the $l = 2$ is still the largest contribution, but $l = 4$ has a significant contribution throughout the merger and $l = 6$ and $l = 8$ close to the maximum.

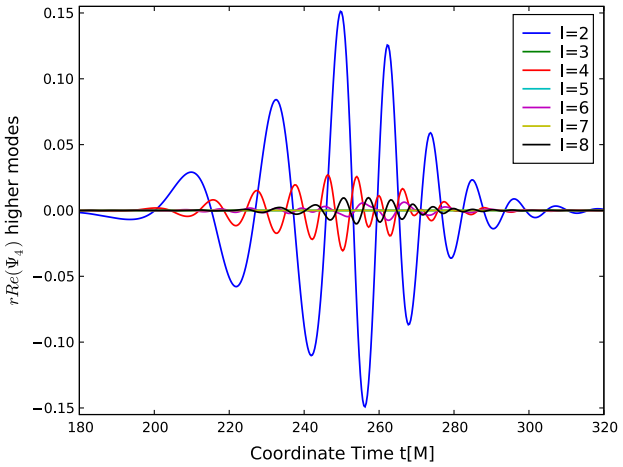

FIG. 13 (color online). Higher modes of $r\mathcal{R}e(\Psi_4)$ summed over m for the $P = 1P_{\rm qc}$, $\Theta = 47°$, equal-mass case. Clearly one can see that $l = 2$ modes are—just as in the quasicircular case—the dominant contribution. The plot also reveals that the GW emission has a much more significant contribution from higher-l modes compared to a quasicircular binary. All odd-l modes vanish within numerical error as expected from the quadrant symmetry of equal-mass, nonspinning BHBs.

As an example of how different waveforms of binaries with eccentricities and mass ratios away from unity can be, we show in Fig. 24 the waveform and orbital trajectories for the mass ratio 1:3. Clearly the features induced by an eccentric unequal-mass BHB give rise to waveforms which effectively break degeneracies in parameter space [33,101].

In this work we do not construct waveform templates. Longer runs will be needed in order to achieve a match to a PN waveform because of the small separations at pericenter. Performing wave extraction at larger radii is also clearly desirable in this context. With current codes this could be done at an acceptable computational cost.

2. Radiated energy

We compute the energy $E_{\rm rad}$ radiated away in GWs and analyze these results together with the orbital dynamics. For the elliptic orbits we add an estimate of the radiated energy of the past evolution $E_{\rm rad}^{\rm past} \approx -E_{\rm bind}(t = 0)$ to $E_{\rm rad}$. Using this estimate we implicitly assume that the binary was isolated in its entire past. The actual value $E_{\rm bind}(t = 0)$ for the $P = P_{\rm qc}$ sequence turns out to be $E_{\rm rad}^{\rm past} \approx -E_{\rm bind}(t = 0) \approx 0.0057 \pm 0.0001$. We normalize $E_{\rm rad}$ by the ADM mass of the initial time slice, $M_{\rm ADM}(t = 0)$. The resulting quantity is what we call the "efficiency" of gravitational radiation.

The results of all our evolutions are presented in Figs. 14–17 and 24. The different lines (colors, symbols) in these plots correspond to different initial momenta and each line shows the efficiency of gravitational radiation as a function of Θ.

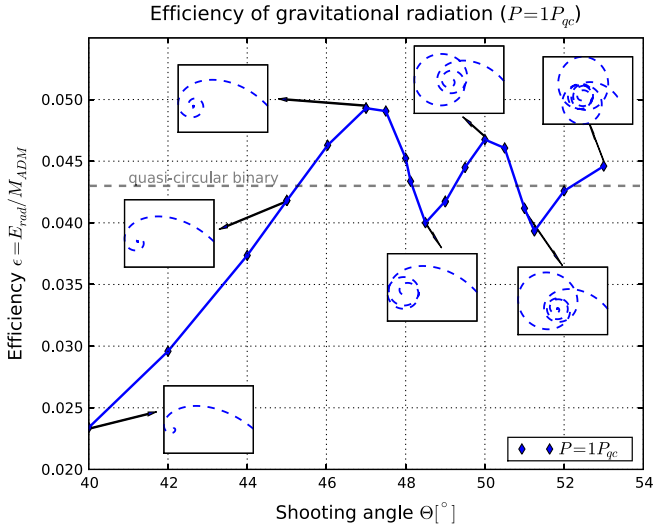

FIG. 14 (color online). Radiated energy as a function of the shooting angle Θ for the $P = 1P_{\rm qc}$ runs. The small insets illustrate the corresponding orbital dynamics. One can see that the global maximum does *not* correspond to a zoom-whirl orbit. Rather, the strongest zoom-whirl behavior is associated with the local *minimum* in $E_{\rm rad}$ near $\Theta = 48.5°$. (Compare this to the cases that show plateaus in Fig. 12.) Note that the case 48.5° is fairly similar to the 48° case shown in Fig. 5, consistent with our conclusion from Ref. [24] that the degree of fine-tuning to see zoom-whirls is on the order of 1%.

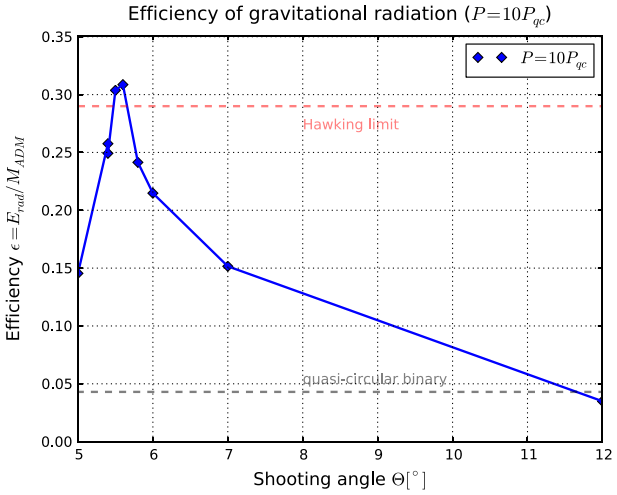

FIG. 16 (color online). Radiated energy for $P = 10P_{\rm qc}$ (i.e., $P \approx 0.6M$). The values for Θ are not comparable with those from the other P sequences as the initial separation was chosen to be $D(t = 0) = 50M$ due to the large junk radiation. Only at $P = 10P_{\rm qc}$ are we able to exceed the Hawking limit [106] on the energy release of two Schwarzschild BHs far apart without orbital angular momentum. With $P = 10P_{\rm qc}$ the spacetime is very different from Schwarzschild. Note that the results are below the current maximum reported value of $35 \pm 5\%$. The contribution from junk radiation is about 0.05 and is included in the data shown. (In the case $\Theta = 12°$ it is slightly lower.)

The first global feature to notice is that gravitational radiation becomes much more efficient for higher momenta. We give the maximal efficiency for seven initial momenta P. So far the largest value, $35 \pm 5\%$, was reported in Refs. [21,38,40,102] (in which the punctures have coordinate velocities of $v = 0.94$). In our data set we come rather close to this limit (see Fig. 16). The challenge in these studies arises from the growing significance of unphysical radiation content that is associated with the construction of initial data. Here we did not intend to push this limit further, but this shows that we have probed part of the parameter space close to the limits of former investigations. As we shall demonstrate (see Fig. 17), the sampling is quite exhaustive and allows us to probe zoom-whirl behavior in a large class of orbits. In particular, one of our important findings is the model $P = 1P_{\rm qc}$, $\Theta = 60°$ (elliptic class) with several close encounters before merger; see Fig. 7. The initial eccentricity is as low as $e \sim 0.5$. This is a value within typical estimates of supermassive BHBs in galaxy-merger scenarios following star- or disk-driven hardening [50], and it is also a value found for inspiraling binaries near galactic cores [65] which are driven to very similar eccentricities via the Kozai mechanism.

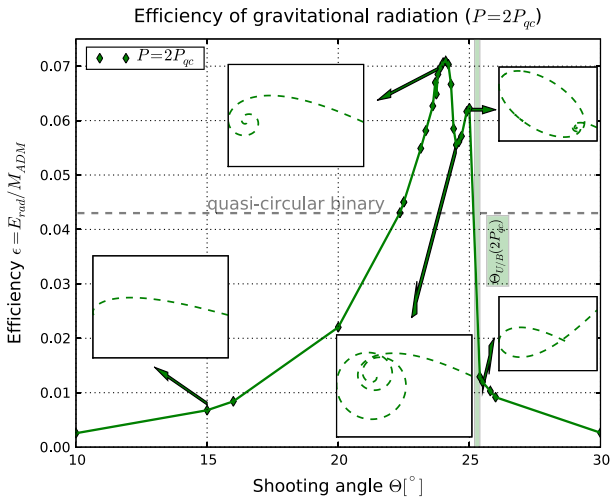

FIG. 15 (color online). Radiated energy for $P = 2P_{\rm qc}$. While in the $P = 1P_{\rm qc}$ case there are multiple extrema we find only two maxima here. Note the fine sampling around the extrema. The rather large gap around $\Theta_{U/B} \equiv \Theta_{\rm bu}$ reflects the problem visible in the upper right inset and in Fig. 22, namely that the BHs zoom out to very large distances, which implies large t_m and consequently high computational costs (also due to the requirement of higher resolution).

For low momenta and the mass ratios under consideration the shooting angles for the largest number of orbits in general neither coincide with the maxima in $E_{\rm rad}$ nor do they coincide with the unstable, circular (whirl-like) orbits merging immediately thereafter. Generally, the maximum in $E_{\rm rad}$ inside the hyperbolic regime lies close to the merger/fly-by threshold. However, in the limit $P \to \infty$ there appears to be a growing amount of degeneracy: the unstable circular orbits actually seem to coincide with the

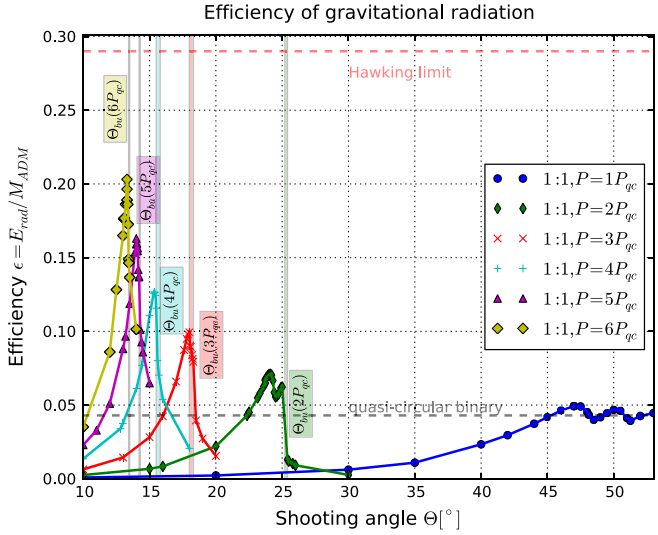

FIG. 17 (color online). Radiated energy for the 1qc–6qc runs (i.e., $0.06M \leq P \leq 0.36M$) including the values corresponding to a quasicircular binary and the Hawking limit. The vertical lines mark $\Theta_{\rm bu}$ for each momentum scale considered. This value is close but not identical to the threshold of immediate merger. As expected the shooting angle where zoom-whirls occur is closer to the $\Theta = 0$ (head-on) case for higher initial momentum. The higher the initial momentum, the greater the radiated energy. In the $1P_{\rm qc}$ sequence we have not included the data for $\Theta = 60°$, but the efficiency of radiation agrees within plotting accuracy with the value for a quasicircular BHB, as expected from extrapolating the data set shown.

most efficient radiators. In the next section we will give an interpretation for this behavior.

For low Θ we find, in agreement with previous studies [21], that the radiated energy quickly drops to the small amounts known from head-on collisions [40]. This drop can clearly be seen for every initial momentum considered in Fig. 17.

In addition, the shape of the transition from large to small Θ is by no means trivial. One of the key features in the radiated energy is that, especially in the $P = 1P_{\rm qc}$ sequence but also for $P = 2P_{\rm qc}$, there appear additional local extrema which match the number of encounters. The observed structure in $E_{\rm rad}$ shows a remarkably clean periodicity as a function of Θ and should be compared with corresponding features in the final spin and mass in Ref. [25]. We find that these features in $E_{\rm rad}$ are determined entirely by the dynamics during the last encounter. Zoom-whirl effects in the $P = 1P_{\rm qc}$ sequence *minimize* radiated energy. We find that the radiated energy is *less* than that of a quasicircular binary, in direct contrast to Ref. [92]. We will interpret these observations in the next section.

Looking at our findings presented in Figs. 15 and 17, one may wonder why the additional peaks, i.e., additional encounters, are present in the lowest-momentum sequence, but not in the higher-momentum ones. The answer lies in the initial binding energy. For the large-P cases only those evolutions which radiate a lot of energy during the first encounter will be bound orbits (dynamical captures). As it turns out, the radius of capture for these evolutions is inside the ISCO of a single Schwarzschild black hole of the same total mass. The capturing encounter generically is a whirl and thus an unstable orbit. After the BHs are dynamically captured they will have lost additional angular momentum and energy. Thus the pericenter distance on their next encounter will be even smaller and therefore will always end in a merger.

Another observation is that in the $P = 2P_{\rm qc}$ sequence there is a second peak next to the global maximum, in contrast to the higher-P sequences. The peak arises from contributions during the second (and last) encounter. While we also observe similar orbital dynamics for the higher-P cases, we however do not see a corresponding peak. The reason is obvious once one compares the GW amplitudes during the capturing first encounter with the amplitude during merger; see Figs. 8 and 9. For the large-P evolutions the mergers on the second encounter only have a negligible contribution to the radiated energy, but the whirly, capturing encounter dominates the energy loss.

Results for unequal-mass runs are shown in Fig. 18. According to our findings the scaling of radiated energy with mass ratio is eccentricity dependent. Comparing the maxima in $E_{\rm rad}$ between equal-mass and unequal-mass runs, we find that a mass ratio of 1:2 still gives a maximal efficiency which is not too far away from the corresponding equal-mass run with the same $P/M_{\rm ADM}$. This result is in contradiction to our expectation from quasicircular

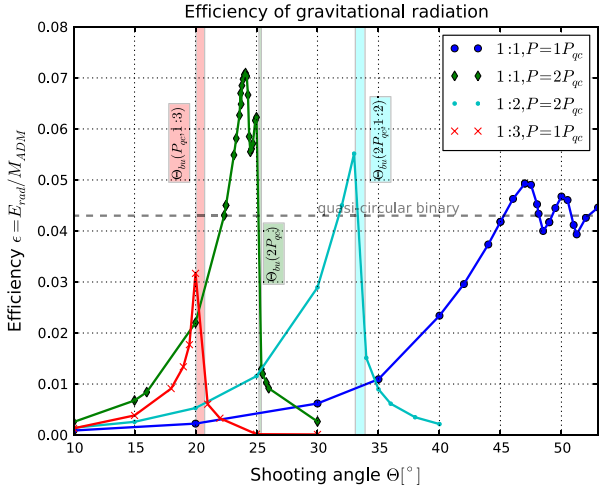

FIG. 18 (color online). Radiated energy $E_{\rm rad}$ for mass ratios 1:1, 1:2, and 1:3 and some particular values of P. Qualitatively the results for unequal masses are similar to those for equal masses. For example, note the drop in $E_{\rm rad}$ after a global maximum; the global maximum corresponds to an orbit that roughly completes one orbit, and zoom-whirl behavior for low P is associated with inefficient radiation as in the equal-mass regime. For $P = 2P_{\rm qc}$, zoom-whirl behavior for a mass ratio of 1:2 occurs for larger Θ than in the 1:1 case.

binaries where $E_{\rm rad}$ decreases steeply with mass ratio. Also, our results for mass ratios of 1:3 show a similar trend, suggesting that such mass ratios are still (in the above sense) far away from the geodesic limit. Our results suggest further parameter studies to analyze the scaling in the eccentric regime along the mass-ratio axis. Clearly, $E_{\rm rad}$ is much more sensitive to P than to ν.

C. New diagnostics

Many interesting questions about BHBs cannot be tackled by just looking at gauge-invariant quantities. In this section we suggest new diagnostics that are helpful to interpret these spacetimes.

A first example is the observation in Ref. [24] that maxima in $E_{\rm rad}$ coincide with a particular orbital configuration at the time of merger. Whenever the tangent vector of the puncture orbits and the separation vector $\vec{D}$ at the time of merger are closest to being orthogonal, the radiated energy is maximized. Here, we also see the same behavior for $P = 2P_{\rm qc}$ orbits. Figure 19 shows two representative cases: a generic case and the one which maximizes $E_{\rm rad}$. This demonstrates the robustness of our gauge-dependent conclusions in Ref. [24].

We interpret this empirical finding in the following way.

We empirically find that it is a good assumption that within each P sequence the velocity and separation at merger are universal; see Figs. 21–23.

Making $\vec{D}$ and $\vec{P}$ orthogonal thus translates into maximizing $\vec{L} = \vec{D} \times \vec{P}$, the Newtonian expression for the angular momentum of two point masses.

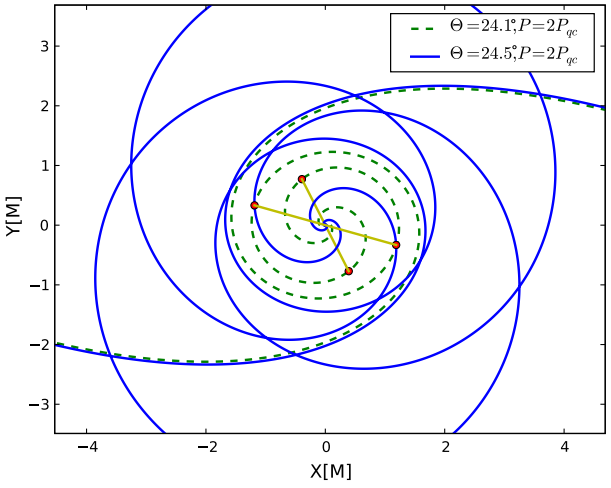

FIG. 19 (color online). The inner region of puncture tracks from two different runs. The $P = 2P_{\rm qc}$, $\Theta = 24.1°$ run (green dashed line) corresponds to the global maximum in $E_{\rm rad}$. The yellow straight lines through the origin represent the separation vectors $\vec{D}$ at the time when a common horizon forms. The result from Ref. [24] that most efficient mergers occur when the tangent vectors of the orbits are closest to being orthogonal to $\vec{D}(t_m)$ carries over to larger P.

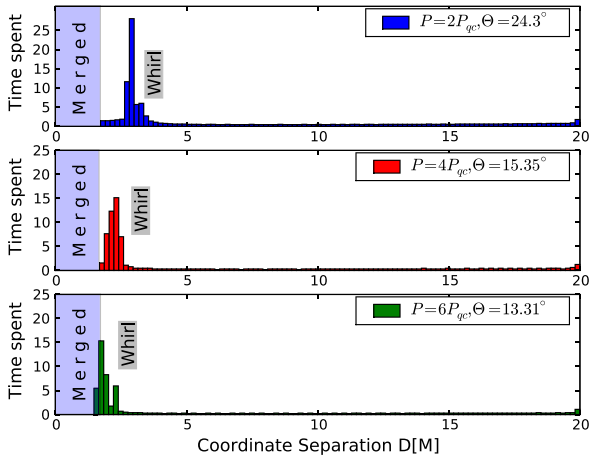

FIG. 20 (color online). Histogram of the coordinate separation D for three different evolutions with $P = 2, 4, 6P_{\rm qc}$. This plot shows how much time a binary has spent at a given separation D. All runs shown here correspond to the longest whirl phase found at each fixed momentum. Clearly visible is the tightening of the whirl radius for larger P (compare with Ref. [24]). The overlap of the shaded region in $P = 6P_{\rm qc}$ with the histogram happens because during the whirl the separation is indeed shorter than at the onset of merger.

We therefore conjecture based on our data set that the strongest ring-down signals are caused by those evolutions which maximize the angular momentum at the moment of merger.

Another useful diagnostic is the histogram of $D(t)$ (see Fig. 20 and Ref. [24]). It measures the time the binary

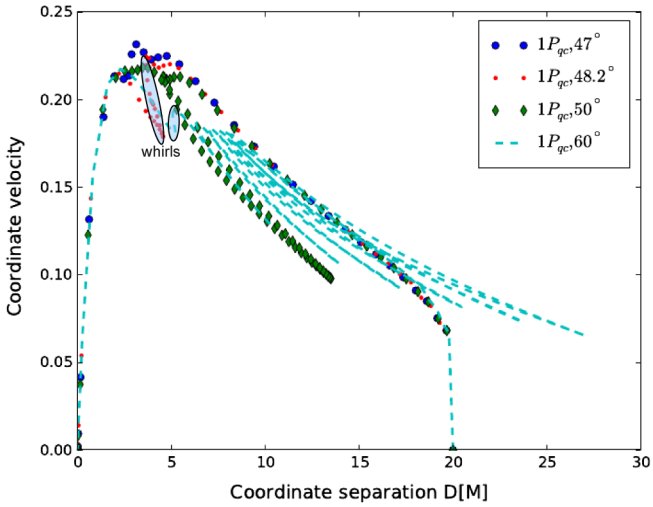

FIG. 21 (color online). Phase space for $P = 1P_{\rm qc}$ sequence. The $\Theta = 48.2°$ evolution takes a detour in phase space, thereby avoiding the region where radiation is most efficient. The $\Theta = 47°$ evolution radiates more efficiently because it reaches further towards the upper left and at the same time spends considerable time at low D (see Fig. 6 in Ref. [24]). Merger occurs at $D(t_{\rm merger}) \sim 2M$.

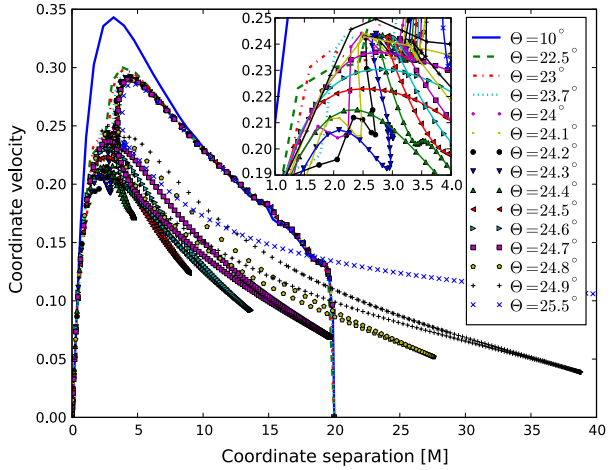

FIG. 22 (color online). Phase space for $P = 2P_{\rm qc}$ sequence. All runs except $\Theta = 25.5°$ are bound. Near the threshold of immediate merger the zooms ($24.3° \lesssim \Theta \lesssim 24.9°$) may extend farther out. The inset shows a close-up of the inner region where (i) trajectories from binaries that survive the first encounter depart from those that do not and (ii) whirls occur (the point density is enlarged there). Merger occurs at $D(t_{\rm merger}) \sim 2M$.

spends within an interval $D \pm \Delta D$ of coordinate separation. We focus on two important conclusions drawn from this plot. First, as already reported in Ref. [24] the whirls show up as a sharp and well-defined peak, allowing us to measure the radii of unstable circular orbits in these highly nonlinear spacetimes. Second, the whirl radii become

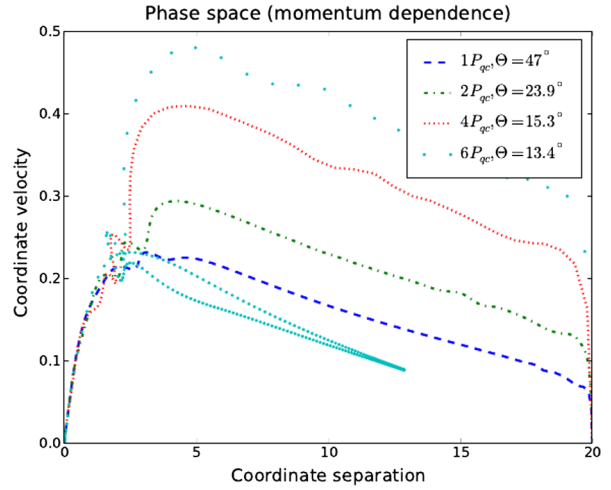

FIG. 23 (color online). Phase space for different initial momenta P with angles chosen for near maximal $E_{\rm rad}$. Interestingly, if Θ is chosen for maximum radiative efficiency, then close to the merger *all* binaries reach the same coordinate velocity independent of the large differences in initial conditions. This effect appears as a blurred "focal" point in phase space. Hence the whirl itself becomes more important for $E_{\rm rad}$ than the actual merger. The deceleration in the $6P_{\rm qc}$ whirl phase is larger than during the merger. Merger occurs at $D(t_{\rm merger}) \lesssim 2M$.

systematically tighter as P increases (see Fig. 20), which is related to a higher Kerr parameter of the merger remnant [21,26]. We checked the coordinate separation as a function of time separately to exclude a possible issue with our merger-time estimate, which is not well suited for large P.

For low momenta, Refs. [23,25] showed that the final spin parameter lies within $0.6 < a < 0.832$ with the tendency that the spin parameter grows with the initial momentum. Thus for larger P the resulting background spacetime will have a tighter ISCO. As the binary spends considerably more time at the whirl radius than at a Newtonian pericenter at the same distance (see Fig. 20) the binary radiates much more efficiently if this whirl occurs at a smaller radius. Thus the geodesic analog together with our gauge-dependent diagnostics give a natural explanation for our earlier observations: in the high-momentum case zoom-whirl orbits do coincide with the most efficient radiators where the whirls are tight, while this is not the case in the low-momentum regime, where the whirl radii are significantly larger.

As a final diagnostic we present trajectories of the binaries through phase space; see Figs. 21–24. We choose $D(t)$ and the coordinate velocity $v(t)$ of the punctures as generalized coordinates. This construction is explicitly coordinate dependent, and switching to another gauge will lead to different trajectories. However, previous investigations led to the conclusion that the moving puncture

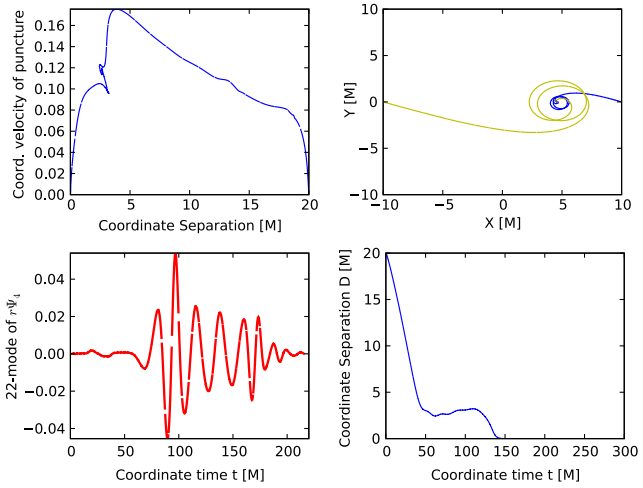

FIG. 24 (color online). Mass ratio 1:3, $\Theta = 20°$, $P = P_{\rm qc}$: Phase-space trajectory (upper left), orbital tracks (upper right), 22-mode of $r\Psi_4$ (lower left), and coordinate separation as a function of time (lower right). The whirl phase is slightly but not significantly longer than that for the equal-mass configuration. Compare the decrease in velocity (deceleration) during the final plunge shown in the phase-space trajectory with the equal-mass cases shown in Figs. 21–23. These differences can be understood by comparing the radiation efficiencies of these systems. A comparison of the 22-mode to the equal-mass runs suggests a strong sensitivity to the mass ratio. Note that the merger is not the strongest signal in Ψ_4.

gauge leads to puncture tracks that correspond rather well to what an observer sees from infinity (see, e.g., Refs. [73,88,103]). In particular, for orbiting motion one can argue based on the shift condition that this should be the case [88], although for linear motion the situation is different. Hence, one has to keep the gauge issue in mind, but the moving puncture gauge leads to rather robust features in the phase-space trajectories, as we will discuss next.

To familiarize oneself with the trajectories in phase space, consider a circular motion with constant velocity. This motion corresponds to a single point in a D-v phase-space diagram. A Kepler ellipse corresponds to a line, which is curved according to Kepler's third law.

In Fig. 21 we show runs for $P = 1P_{\rm qc}$ for four different Θ, while Fig. 22 gives a global impression of many different angles for $P = 2P_{\rm qc}$ (each for equal masses). These simulations start at the lower right corner at $D = 20M$, $v = 0$ and quickly rise due to the initial gauge adjustment, so that the coordinate velocity of each BH approaches the value expected from the initial data. Then the trajectory moves towards the upper left as the orbits shrink and the punctures move faster. When the black holes merge the trajectory ends at the origin at $D = 0$, $v = 0$. Whirls or parts of tight circular orbits are indicated by approximately constant D but decreasing v, with $D \approx 2M$–$5M$. Zooms follow roughly the shape of elliptic orbits, with D varying between $5M$–$10M$ at pericenter out to an apocenter at $15M$–$27M$ in Fig. 21 or up to $40M$ in Fig. 22. Also shows one orbit for $P = 2P_{\rm qc}$ which escapes to infinity. The inset demonstrates that the coordinate velocity at mergers varies by $\Delta v_m \sim \pm 0.02$ for evolutions near the capture threshold. For head-on collisions the value can be significantly larger.

A head-on collision in phase space looks very much like an eccentric binary starting on the $v = 0$ line at the value of D that corresponds to the same total energy. We note that a head-on collision always constitutes an upper envelope in the phase space, i.e., by fixing P and comparing $\Theta = 0$ runs with $\Theta \neq 0$ evolutions we always find $v(t, \Theta = 0) > v(t, \Theta \neq 0)$ [at least for $D(t) \leq D(t = 0)$].

We note that for orbits which maximize the radiative efficiency the motion of the punctures at the onset of merger is still rather mildly relativistic. This finding turns out to be surprisingly insensitive to the initial momentum. Figure 23 shows runs for different P with angles chosen for maximum radiation efficiency. Increasing the initial momentum of the punctures leads to a motion which is rather relativistic when entering the whirl phase, up to $v \sim 0.5$ and a Lorentz factor $W \sim 1.155$ for $P = 6P_{\rm qc}$ (see Fig. 23), but in the whirl they decelerate by large amounts (for $P = 6P_{\rm qc}$ the decrease in velocity is as large as during the merger). At merger, however, *all* equal-mass evolutions which maximize radiative efficiency approach $v = 0.22 \pm 0.02$ or $W = 1.025 \pm 0.005$.

For a detailed look at the transition zone between bound and unbound evolutions, see Fig. 22 for the $P = 2P_{\rm qc}$ sequence with varying Θ. First, we recognize the two extreme cases of merger and unbound motion. In between we find a very complex transition which is governed by several additional (nonclosed) loops corresponding to orbits that zoom out after a first whirl phase, thereby slowing down (i.e., moving to the lower right) before returning towards the upper left. Note that during the next approach the binary must follow a path further to the lower left because the system is dissipative. The set of apocenters from all runs in this sequence forms a lower envelope (similar to the upper envelope mentioned before) that is never crossed by any of our evolutions at the same initial D. Note how far the zooms may extend when the binary approaches the merger/fly-by threshold, resulting in an ever larger runtime in agreement with the geodesic case. We face difficulties evolving orbits near $\Theta \to \Theta^{\rm merger}_{\rm fly\text{-}by}$ because these orbits need very long evolutions (decrease of accuracy) and the black holes may reach distances close to or even beyond the wave extraction sphere, thereby producing artificial features in $E_{\rm rad}$.

An investigation of the phase-space trajectories of unequal-mass BHBs reveals that the general shape of the trajectories is quite robust with respect to the mass ratio. An example is given in Fig. 24. With regard to gravitational radiation, unequal-mass binaries do not tap as deeply into the gravitational potential as equal-mass binaries, and thus they cannot extract as much energy from the spacetime. There are two basic differences. (i) Unequal-mass orbits move systematically slower compared to a corresponding equal-mass binary with comparable initial momentum. (ii) Unequal-mass mergers start their final plunge from an increasingly larger coordinate separation and at lower coordinate velocity than equal-mass mergers. For higher mass ratios, the difference in coordinate velocity between plunge and just after merger (deceleration) is milder and the GW signals are weaker; see Fig. 24. This is qualitatively consistent with earlier head-on studies [40]. This behavior bears resemblance to the radiation of an accelerated charge in electromagnetism.

IV. CONCLUSIONS

Numerical relativity has confirmed the existence of zoom-whirl orbits beyond the geodesic, extreme-mass-ratio, and PN regimes [20–24,26,27], thereby emphasizing their universality by including the regime of comparable masses where radiation losses become significant. Previous studies explored the rich extension to the phenomenology of the GR two-body problem offered by zoom-whirl dynamics in various ways. In this work we performed numerical relativity simulations to investigate the parameter space of comparable-mass, nonspinning, eccentric BHBs for low and intermediate momenta more comprehensively than before. We explored zoom-whirl behavior

in both the hyperbolic and elliptic regimes, carrying out more than 100 numerical evolutions in order to obtain a decent sampling of the underlying parameter space. We discussed various features of the orbits and characterized the corresponding GW emission, and we developed new diagnostics to analyze binary spacetimes by using phase-space trajectories and a histogram of the coordinate separation.

For elliptic orbits, we discovered zoom-whirls with imprints in the GWs that are comparable in amplitude to the merger waveform for eccentricities as low as $e \sim 0.5$. This is an important finding for the astrophysical relevance of zoom-whirl orbits. In particular, such values are within expected eccentricities of supermassive BHBs that have resulted from galaxy mergers and subsequent star- or gas-driven hardening [50]. For low momenta, there occur several minima and maxima in the radiated energy when varying the shooting angle from head-on to quasicircular orbits. We demonstrated that zoom-whirl dynamics may actually *minimize* the radiated energy, in sharp contrast to Ref. [43].

In the elliptic regime whirls are found only during their last encounter. They emerge in *disjoint* intervals of the initial angular momentum (i.e., shooting angle). Apparently, as long as the binaries are not circularized just prior to plunge, zoom-whirls can always be found during the last encounter by a very modest amount of fine-tuning. In the hyperbolic regime we find that all evolutions that lead to dynamical capture reveal whirl features during the capturing encounter and then simply plunge during the following encounter, potentially from a large separation.

High-momentum zoom-whirls maximize the radiated energy. The Kerr spacetime that the merger remnant will settle down to exhibits a larger spin parameter than is observed for lower momenta. This translates into a tighter unstable circular orbit (i.e., the whirl radius), resulting in more pronounced dynamics of the mass quadrupole. In particular, the first, capturing close-encounter burst in high-momentum evolutions can easily overwhelm the merger signal.

In the unequal-mass case eccentric BHBs are found to be more efficient radiators than expected from quasicircular studies of unequal-mass BHBs. As a consequence the whirls for larger mass ratios are not significantly longer than in the equal-mass case for the mass ratios under consideration. We note that numerical relativity is seeing improvements in dealing with large mass ratios [104,105]. More detailed studies for unequal masses and also the inclusion of spin are promising directions for eccentric BHB simulations in the future.

The present work as well as other studies strongly suggest including eccentricity in the waveform templates used in the data analysis of GW detectors, since eccentricity effectively breaks degeneracies in parameter space.

ACKNOWLEDGMENTS

We are grateful to David Hilditch, Sebastiano Bernuzzi, Ulrich Sperhake, Frans Pretorius, Luis Lehner, Deirdre Shoemaker, Doreen Müller, Norbert Lages, and Marcus Thierfelder for discussions, and we also thank Marcus Thierfelder for giving us access to his event-horizon finder. This work was supported in part by grants DFG GK 1523, DFG SFB/Transregio 7, and DLR LISA Germany at the Friedrich-Schiller University Jena, as well as NSF Grant PHY-0963136, and NASA Grant NNX11AE11G at the University of Illinois at Urbana-Champaign. Computations were performed at LRZ Munich.

[1] K. Glampedakis and D. Kennefick, Phys. Rev. D **66**, 044002 (2002).
[2] The term zoom-whirl is attributed to C. Cutler and E. Poisson (who in turn mention that it was suggested by K. Thorne).
[3] R. A. Hulse and J. H. Taylor, Astrophys. J. **195**, L51 (1975).
[4] M. Burgay *et al.*, Nature (London) **426**, 531 (2003).
[5] M. Kramer *et al.*, Science **314**, 97 (2006).
[6] A. Sillanpaa, S. Haarala, M. Valtonen, B. Sundelius, and G. Byrd, Astrophys. J. **325**, 628 (1988).
[7] M. J. Valtonen, S. Mikkola, D. Merritt, A. Gopakumar, H. J. Lehto, T. Hyvönen, H. Rampadarath, R. Saunders, M. Basta, and R. Hudec, Astrophys. J. **709**, 725 (2010).
[8] J. Levin, S. McWilliams, and H. Contreras, Classical Quantum Gravity **28**, 175001 (2011).
[9] S. Chandrasekhar, *The Mathematical Theory of Black Holes* (Oxford University Press, USA, 1983).
[10] C. Cutler, D. Kennefick, and E. Poisson, Phys. Rev. D **50**, 3816 (1994).
[11] K. Martel, Phys. Rev. D **69**, 044025 (2004).
[12] J. Levin and G. Perez-Giz, Phys. Rev. D **77**, 103005 (2008).
[13] S. Drasco and S. A. Hughes, Phys. Rev. D **73**, 024027 (2006).
[14] R. Haas, Phys. Rev. D **75**, 124011 (2007).
[15] L. Barack and N. Sago, Phys. Rev. D **81**, 084021 (2010).
[16] J. Levin and B. Grossman, Phys. Rev. D **79**, 043016 (2009).
[17] R. Grossman and J. Levin, Phys. Rev. D **79**, 043017 (2009).
[18] S. A. Hughes, S. Drasco, E. E. Flanagan, and J. Franklin, Phys. Rev. Lett. **94**, 221101 (2005).
[19] M. E. Pati and C. M. Will, Phys. Rev. D **65**, 104008 (2002).

[20] F. Pretorius and D. Khurana, Classical Quantum Gravity **24**, S83 (2007).
[21] U. Sperhake, E. Berti, V. Cardoso, J. A. González, B. Brügmann, and M. Ansorg, Phys. Rev. D **78**, 064069 (2008).
[22] I. Hinder, B. Vaishnav, F. Herrmann, D. Shoemaker, and P. Laguna, Phys. Rev. D **77**, 081502 (2008).
[23] M. C. Washik, J. Healy, F. Herrmann, I. Hinder, D. M. Shoemaker, P. Laguna, and R. A. Matzner, Phys. Rev. Lett. **101**, 061102 (2008).
[24] R. Gold and B. Brügmann, Classical Quantum Gravity **27**, 084035 (2010).
[25] J. Healy, P. Laguna, R. A. Matzner, and D. M. Shoemaker, Phys. Rev. D **81**, 081501 (2010).
[26] J. Healy, J. Levin, and D. Shoemaker, Phys. Rev. Lett. **103**, 131101 (2009).
[27] J. Healy, F. Herrmann, I. Hinder, D. M. Shoemaker, P. Laguna, and R. A. Matzner, Phys. Rev. Lett. **102**, 041101 (2009).
[28] K. Martel and E. Poisson, Phys. Rev. D **60**, 124008 (1999).
[29] K. Martel, AIP Conf. Proc. **493**, 48 (1999).
[30] D. A. Brown and P. J. Zimmerman, Phys. Rev. D **81**, 024007 (2010).
[31] T. Cokelaer and D. Pathak, Classical Quantum Gravity **26**, 045013 (2009).
[32] B. Vaishnav, I. Hinder, D. Shoemaker, and F. Herrman, Classical Quantum Gravity **26**, 204008 (2009).
[33] B. Mikoczi, B. Kocsis, P. Forgacs, and M. Vasuth, Phys. Rev. D **86**, 104027 (2012).
[34] W. E. East and F. Pretorius, Astrophys. J. Lett. **760**, L4 (2012).
[35] W. E. East, F. Pretorius, and B. C. Stephens, Phys. Rev. D **85**, 124009 (2012).
[36] R. Gold, S. Bernuzzi, M. Thierfelder, B. Brügmann, and F. Pretorius, Phys. Rev. D **86**, 121501(R) (2012).
[37] B. C. Stephens, W. E. East, and F. Pretorius, Astrophys. J. **737**, L5 (2011).
[38] M. Shibata, H. Okawa, and T. Yamamoto, Phys. Rev. D **78**, 101501 (2008).
[39] U. Sperhake, V. Cardoso, F. Pretorius, E. Berti, T. Hinderer, and N. Yunes, Phys. Rev. Lett. **103**, 131102 (2009).
[40] U. Sperhake, V. Cardoso, F. Pretorius, E. Berti, and J. A. González, Phys. Rev. Lett. **101**, 161101 (2008).
[41] E. Berti, V. Cardoso, T. Hinderer, M. Lemos, F. Pretorius, U. Sperhake, and N. Yunes, Phys. Rev. D **81**, 104048 (2010).
[42] E. Berti, V. Cardoso, T. Hinderer, M. Lemos, F. Pretorius, U. Sperhake, and N. Yunes, Phys. Rev. D **81**, 104048 (2010).
[43] P. C. Peters, Phys. Rev. **136**, B1224 (1964).
[44] A. Sesana, C. Roedig, M. Reynolds, and M. Dotti, arXiv:1107.2927.
[45] F. Khan, A. Just, and D. Merritt, Astrophys. J. **732**, 89 (2011).
[46] M. Preto, I. Berentzen, P. Berczik, and R. Spurzem, arXiv:1102.4855.
[47] J. C. B. Papaloizou, R. P. Nelson, and F. Masset, Astron. Astrophys. **366**, 263 (2001).
[48] P. J. Armitage and P. Natarajan, Astrophys. J. **634**, 921 (2005).
[49] J. Cuadra, P. Armitage, R. Alexander, and M. Begelman, Mon. Not. R. Astron. Soc. **393**, 1423 (2009).
[50] C. Roedig and A. Sesana, J. Phys. Conf. Ser. **363**, 012035 (2012).
[51] S. Portegies Zwart and S. McMillan, Astrophys. J. Lett. **528**, L17 (2000).
[52] M. Benacquista, S. F. Portegies Zwart, and F. Rasio, Classical Quantum Gravity **18**, 4025 (2001).
[53] L. Wen, Astrophys. J. **598**, 419 (2003).
[54] D. Pooley *et al.*, Astrophys. J. **591**, L131 (2003).
[55] M. C. Miller and D. P. Hamilton, Astrophys. J. **576**, 894 (2002).
[56] W. H. Lee, E. Ramirez-Ruiz, and G. van de Ven, Astrophys. J. **720**, 953 (2010).
[57] R. M. O'Leary, B. Kocsis, and A. Loeb, Mon. Not. R. Astron. Soc. **395**, 2127 (2009).
[58] W. R. Brown, arXiv:0811.0571.
[59] S. Portegies Zwart, H. Baumgardt, S. L. W. McMillan, J. Makino, P. Hut, and T. Ebisuzaki, Astrophys. J. **641**, 319 (2006).
[60] O. Blaes, M. H. Lee, and A. Socrates, Astrophys. J. **578**, 775 (2002).
[61] C. Hopman and T. Alexander, Astrophys. J. **629**, 362 (2005).
[62] I. Mandel, D. A. Brown, J. R. Gair, and M. C. Miller, Astrophys. J. **681**, 1431 (2008).
[63] M. Iwasawa, Y. Funato, and J. Makino, Astrophys. J. **651**, 1059 (2006).
[64] M. Volonteri, F. Haardt, and P. Madau, Astrophys. J. **582**, 559 (2003).
[65] F. Antonini and H. Perets, Astrophys. J. **757**, 27 (2012).
[66] I. Kowalska, T. Bulik, K. Belczynski, M. Dominik, and D. Gondek-Rosinska, Astron. Astrophys. **527**, A70 (2011).
[67] B. Kocsis, A. Ray, and S. P. Zwart, Astrophys. J. **752**, 67 (2012).
[68] B. Brügmann, J. A. González, M. Hannam, S. Husa, U. Sperhake, and W. Tichy, Phys. Rev. D **77**, 024027 (2008).
[69] B. Brügmann, W. Tichy, and N. Jansen, Phys. Rev. Lett. **92**, 211101 (2004).
[70] S. Husa, J. A. González, M. Hannam, B. Brügmann, and U. Sperhake, Classical Quantum Gravity **25**, 105006 (2008).
[71] S. Brandt and B. Brügmann, Phys. Rev. Lett. **78**, 3606 (1997).
[72] M. Ansorg, B. Brügmann, and W. Tichy, Phys. Rev. D **70**, 064011 (2004).
[73] M. Campanelli, C. O. Lousto, P. Marronetti, and Y. Zlochower, Phys. Rev. Lett. **96**, 111101 (2006).
[74] J. G. Baker, J. Centrella, D.-I. Choi, M. Koppitz, and J. van Meter, Phys. Rev. Lett. **96**, 111102 (2006).
[75] M. Shibata and T. Nakamura, Phys. Rev. D **52**, 5428 (1995).
[76] T. W. Baumgarte and S. L. Shapiro, Phys. Rev. D **59**, 024007 (1998).
[77] E. Schnetter, Classical Quantum Gravity **27**, 167001 (2010).
[78] R.-M. Memmesheimer and G. Schäfer, Phys. Rev. D **71**, 044021 (2005).
[79] B. Walther, B. Brügmann, and D. Müller, Phys. Rev. D **79**, 124040 (2009).

[80] Generally speaking, if such an orbit is unbound then the black holes separate without close encounter. If they are bound, then after reaching the first apocenter the orbit becomes inward-bound, which in principle is already included for $\Theta \in [0, 90°]$.
[81] W. H. Press, B. P. Flannery, S. A. Teukolsky, and W. T. Vetterling, *Numerical Recipes in C* (Cambridge University Press, New York, 1992), 2nd ed.
[82] D. Müller and B. Brügmann, Classical Quantum Gravity **27**, 114008 (2010).
[83] D. Müller, J. Grigsby, and B. Brügmann, Phys. Rev. D **82**, 064004 (2010).
[84] D. Alic, L. Rezzolla, I. Hinder, and P. Mosta, Classical Quantum Gravity **27**, 245023 (2010).
[85] S. L. Shapiro and S. A. Teukolsky, *Black Holes, White Dwarfs, and Neutron Stars* (John Wiley & Sons, Hoboken, 1983).
[86] M. Thierfelder, diploma thesis, University of Jena, 2008.
[87] M. Thierfelder and B. Brügmann (unpublished).
[88] M. Hannam, S. Husa, D. Pollney, B. Brügmann, and N. Ó Murchadha, Phys. Rev. Lett. **99**, 241102 (2007).
[89] B. Reimann and B. Brügmann, Phys. Rev. D **69**, 124009 (2004).
[90] M. Alcubierre, *Introduction to* 3 + 1 *Numerical Relativity* (Oxford University Press, USA, 2008).
[91] E. Berti, V. Cardoso, J. A. González, U. Sperhake, and B. Brügmann, Classical Quantum Gravity **25**, 114035 (2008).
[92] P. C. Peters and J. Mathews, Phys. Rev. **131**, 435 (1963).
[93] M. Tessmer and G. Schäfer, Ann. Phys. (Amsterdam) **523**, 813 (2011).
[94] I. Hinder, F. Herrmann, P. Laguna, and D. Shoemaker, Phys. Rev. D **82**, 024033 (2010).
[95] J. Hough, in Edoardo Amaldi Meeting on Gravitational Wave Experiments, Rome, Italy, 1994 (to be published).
[96] S. Babak, M. Hannam, S. Husa, and B. Schutz, arXiv:0806.1591.
[97] P. Amaro-Seoane *et al.*, arXiv:1201.3621.
[98] K. Yagi, Classical Quantum Gravity **29**, 075005 (2012).
[99] M. Hannam and I. Hawke, Gen. Relativ. Gravit. **43**, 465 (2011).
[100] C. Van Den Broeck, in *Proceedings of the Twelfth Marcel Grossmann Meeting on General Relativity Paris, France, 2009*, edited by T. Damour, R. T. Jantzen, R. Ruffini (World Scientific, Singapore, 2012), p. 1682.
[101] J. S. Key and N. J. Cornish, Phys. Rev. D **83**, 083001 (2011).
[102] U. Sperhake, Lect. Notes Phys. **769**, 125 (2009).
[103] P. Diener, F. Herrmann, D. Pollney, E. Schnetter, E. Seidel, R. Takahashi, J. Thornburg, and J. Ventrella, Phys. Rev. Lett. **96**, 121101 (2006).
[104] C. O. Lousto and Y. Zlochower, Phys. Rev. Lett. **106**, 041101 (2011).
[105] J. A. González, U. Sperhake, and B. Brügmann, Phys. Rev. D **79**, 124006 (2009).
[106] S. Hawking, Phys. Rev. Lett. **26**, 1344 (1971).